BASE - Annual Report 2021

Stefan Ulmer[1], *Christian Smorra*[1,2], *Jack A. Devlin*[1,3], *Barbara M. Latacz*[1,4], *Peter Micke*[1,3], *Elise Wursten*[1,4], *Matthias J. Borchert*[1,5,6], *Stefan Erlewein*[1,4], *Markus Fleck*[1,7], *Philip Geissler* [1], *Julia I. Jäger*[1,3,4], *Phil Nuschke* [1,6], *Gilbertas Umbrazunas*[1,8], *Frederik Völksen*[1,9], *Fatma. Abbass*[2], *Matthew A. Bohman*[1,4], *Daniel. Popper*[2], *Markus Wiesinger*[4], *Christian Will*[4], *Amado Bautista-Salvador*[5,6], *Julia-Aileen Coenders* [6], *Juan Manuel Cornejo*[5,6], *Teresa Meiners*[5,6], *Johannes Mielke*[5,6], *Julian Pick*[4,5], *Klaus Blaum*[4], *Yasuyuki Matsuda*[7], *Andreas H. Mooser*[4], *Christian Ospelkaus*[5,6], *Wolfgang Quint*[9], *Anna Soter*[8], *Jochen Walz*[2], *Yasunori Yamazaki*[1]

[1]RIKEN, Ulmer Fundamental Symmetries Laboratory, 2-1 Hirosawa, Wako, Saitama, 351-0198, Japan
[2]Institut für Physik, Johannes Gutenberg-Universität, Staudinger Weg 7, D-55128 Mainz, Germany
[3]CERN, Esplanade des Particules 1, CH-1211 Geneva 23, Switzerland
[4]Max-Planck-Institut für Kernphysik, Saupfercheckweg 1, D-69117 Heidelberg, Germany
[5]Physikalisch-Technische Bundesanstalt, Bundesallee 100, D-38116 Braunschweig, Germany
[6]Institut für Quantenoptik, Leibniz Universität Hannover, Welfengarten 1, D-30167 Hannover, Germany
[7]Graduate School of Arts and Sciences, University of Tokyo, 3-8-1 Komaba, Tokyo 153-8902, Japan
[8]Eidgenössisch Technische Hochschule Zürich, Rämistrasse 101, 8092 Zürich, Switzerland
[9]GSI-Helmholtzzentrum für Schwerionenforschung GmbH, Planckstraße 1, D-64291 Darmstadt, Germany

CERN-SPSC-2022-007 / SPSC-SR-304
17/01/2022

Abstract

This report summarizes the progress made by the BASE collaboration in 2021. It contains short summaries of the main output produced, which are three manuscripts published, one in Physical Review Letters [1] and two in Nature [2, 3]. One of these manuscripts sets constraints on the coupling of axions and axion-like particles to photons using the highly sensitive single particle detection systems in the strong magnetic field of the superconducting magnet of the experiment [4, 5]. As a consequence of the successful demonstration of this LC-resonator-based haloscope technique we started constructing the new experiment BASE-CDM. The second manuscript reports on the first demonstration of sympathetic cooling of a single trapped proton by coupling the particle to a cloud of laser-cooled $^9Be^+$ ions using a common-endcap Penning trap method and a superconducting tuned circuit that mediates the cooling [2]. This work was selected by "Physics World" as one of the top ten physics breakthroughs made in 2021. The third manuscript reports on a 16-parts-per-trillion comparison of the proton-to-antiproton charge-to-mass ratio. This measurement improves the previous best limit [6] by a factor of 4.3, and contains the first-ever performed clock-based differential test of the weak equivalence principle with protons and antiprotons. In addition, the group focused on the development and implementation of the new ELENA/BASE interface, and the setup of an experiment dedicated to measure the antiproton magnetic moment with a fractional precision at a level of ≈ 100 parts in a trillion. This includes the setup of a new trap stack, the development of revised cryogenic experiment electronics and superconducting single particle detectors, as well as the implementation of a new magnet shimming system and the development of a cooling trap for sub-thermal cooling cycles at drastically reduced thermalization times.

Contents

1 BASE - Overview

The BASE experiment tests fundamental charge, parity, and time reversal (CPT) invariance by comparing the fundamental properties of protons and antiprotons in advanced cryogenic Penning-trap systems. Experimentally, at the level of known fundamental physics, CPT symmetry is the only combination of discrete symmetry transformations that is observed as an exact symmetry of nature [7]. The results of the experiments conducted by BASE and other collaborations at the AD/ELENA facility are essential in strengthening the assumptions and foundations of relativistic quantum field theory and fundamental physics, and also have great discovery potential for physics beyond the Standard Model.
Based on the first observation of spin flips with a single trapped proton [8] BASE was approved in 2013, since then the following results have been produced:

1. The development of a unique reservoir trap technique, which allows BASE to operate independently from Antiproton Decelerator beam-times.
   Smorra, C. *et al.*, A reservoir trap for antiprotons, *Int. J. Mass Spectrom.* **389**, 10 (2015). [9]
2. First implementation of a "fast shuttling" method, which allows BASE to perform antiproton-to-proton charge-to-mass ratio comparisons with 50 times improved sampling rate compared to traditional single particle mass spectrometers.
   Smorra, C. *et al.*, BASE - The Baryon Antibaryon Symmetry Experiment, *Eur. Phys. J. Special Topics* **224**, 3055 (2015). [10]
3. Comparison of the antiproton-to-proton charge-to-mass ratio with a fractional precision of 69 p.p.t.
   Ulmer, S. *et al.*, High-precision comparison of the antiproton-to-proton charge-to-mass ratio, *Nature* **524**, 196 (2015). [6]
4. The development of ultra-sensitive single particle detection systems with world leading quality [11, 12], tunable quality factors and tunable resonance frequencies.
   Nagahama, H. *et al.*, Highly sensitive superconducting circuits at 700 kHz with tunable quality factors for image-current detection of single trapped antiprotons, *Rev. Sci. Instrum.* **87**, 113305 (2016). [13]
5. The measurement of the antiproton magnetic moment with a fractional precision of 0.8 p.p.m. This improved the previous best determination [14] of the antiproton magnetic moment by a factor of six.
   Nagahama, H. *et al.*, Sixfold improved single particle measurement of the magnetic moment of the antiproton, *Nat. Commun.* **8**, 14084 (2017). [15]
6. The first non-destructive observation of spin flips with a single trapped antiproton. This measurement constitutes the first non-destructive observation of spin quantum transitions in baryonic antimatter.
   Smorra, C. *et al.*, Observation of individual spin quantum transitions of a single antiproton, *Phys. Lett. B* **769**, 1 (2017). [16]
7. The storage of an antiproton cloud for 405 days. This enabled BASE to operate antiproton experiments from November 2015 to December 2016 without antiproton beam consumption. Based on these measurements we improved limits on the directly measured antiproton lifetime by a factor of 7.
   Sellner, S. *et al.*, Improved limit on the directly measured antiproton lifetime, *New J. Phys.* **19**, 083023 (2017). [17]
8. The invention of a new two-particle spectroscopy method for ultra-precise magnetic moment measurements at ultra-high sampling rate.
   Ulmer, S. *et al.*, Challenging the standard model by high-precision comparisons of the fundamental properties of protons and antiprotons, *Phil. Trans. Roy. Soc* **376**, 1 (2018). [18]
9. The measurement of the antiproton magnetic moment with a fractional precision of 1.5 p.p.b. based on the two-particle method. In this measurement, our previous result [15] was improved by a factor

of about 350. Results by other groups [14] were improved by about a factor of 3000.
Smorra, C. *et al.*, A parts-per-billion measurement of the antiproton magnetic moment, *Nature* **550**, 371 (2017). [19]

10. The measurement of the proton magnetic moment with a fractional precision of 0.3 p.p.b., which improved the previous best value, also measured by BASE [20], by a factor of 11. This work constitutes the most precise measurement of the proton magnetic moment to date and improves upon previous best measurements - based on the spectroscopy of atomic hydrogen - by more than a factor of 30.
Schneider, G. *et al.*, Double-trap measurement of the proton magnetic moment at 0.3 parts per billion precision, *Science* **358**, 1081 (2017). [21]
11. The measurement of the lowest cyclotron heating rates ever observed in a trap experiment. Only these ultra-low-noise conditions enable measurements on single proton and antiproton spins.
Borchert, M. *et al.*, Measurement of Ultralow Heating Rates of a Single Antiproton in a Cryogenic Penning Trap, *Phys. Rev. Lett.* **122**, 043201 (2019). [22]
12. The invention of innovative magnetic shielding techniques based on multi-layer shielding systems, which shield certain externally induced magnetic field fluctuation by more than a factor of 200.
Devlin, J.,Wursten, E. *et al.*, Superconducting Solenoid System with Adjustable Shielding Factor for Precision Measurements of the Properties of the Antiproton, *Phys. Rev. Appl.* **12**, 044012 (2019). [23]
13. The derivation of first constraints on antimatter/dark matter interaction, by constraining the coupling of antiproton spins to axion-like dark matter, by studying time-base signatures in antiproton magnetic moment measurements.
Smorra, C. *et al.*, Direct limits on the interaction of antiprotons with axion-like dark matter, *Nature* **575**, 310 (2019). [24]
14. The utilization of the highly sensitive superconducting single particle detection systems of Penning trap experiments to constrain the coupling of axions and axion-like particles to photons.
Devlin, J. A. *et al.*, Constraints on the Coupling between Axionlike Dark Matter and Photons Using an Antiproton Superconducting Tuned Detection Circuit in a Cryogenic Penning Trap, *Phys. Rev. Lett.* **126**, 041301 (2021). [1]
15. The development of novel sympathetic cooling techniques by coupling protons to laser-cooled beryllium ions for magnetic moment measurements at drastically improved sampling rate. In the future, this method will be applied to antiprotons.
Bohman, M. A. *et al.*, Sympathetic cooling of a trapped proton mediated by an LC circuit, *Nature* **596**, 514 (2021). [2]
16. The to date most precise test of CPT invariance with baryons, by comparing the proton/antiproton charge-to-mass ratios with a fractional precision of 16 parts in a trillion. This measurement also constitutes the first differential test of the clock weak equivalence principle with antiprotons.
Borchert, M. J. *et al.*, A 16-parts-per-trillion measurement of the antiproton-to-proton charge–mass ratio, *Nature* **601**, 53 (2022). [3]

For any information beyond the level of detail that is usually published in scientific manuscripts we refer to our annual reports hosted on the CERN document server.
A detailed description of frequency measurements in Penning traps and the current limitations of BASE in the AD facility is given in the BASE future program proposal [25].

2 About this Report

This report summarizes the progress made by the BASE collaboration in 2021. The activities of the group focused on several main topics (see Figure 1), which are the analysis of data accumulated in previous runs and the preparation of related manuscripts, as well as the development of equipment needed for the 2021 antiproton run, such as new electronics for the cryogenic trap system, the implementation of a new cooling trap, the implementation of a magnetic shimming system to tune the precision trap of the experiment to high homogeneity and the implementation of the BASE/ELENA interface. All these developments were implemented with the intention to perform an improved measurement of the antiproton magnetic moment, with better than 5 fold improved precision compared to [19]. From September to November BASE participated in CERN's antiproton run of 2021, we used this period of time to characterize degrader foils for the 2022 antiproton run, the results will be summarized below.

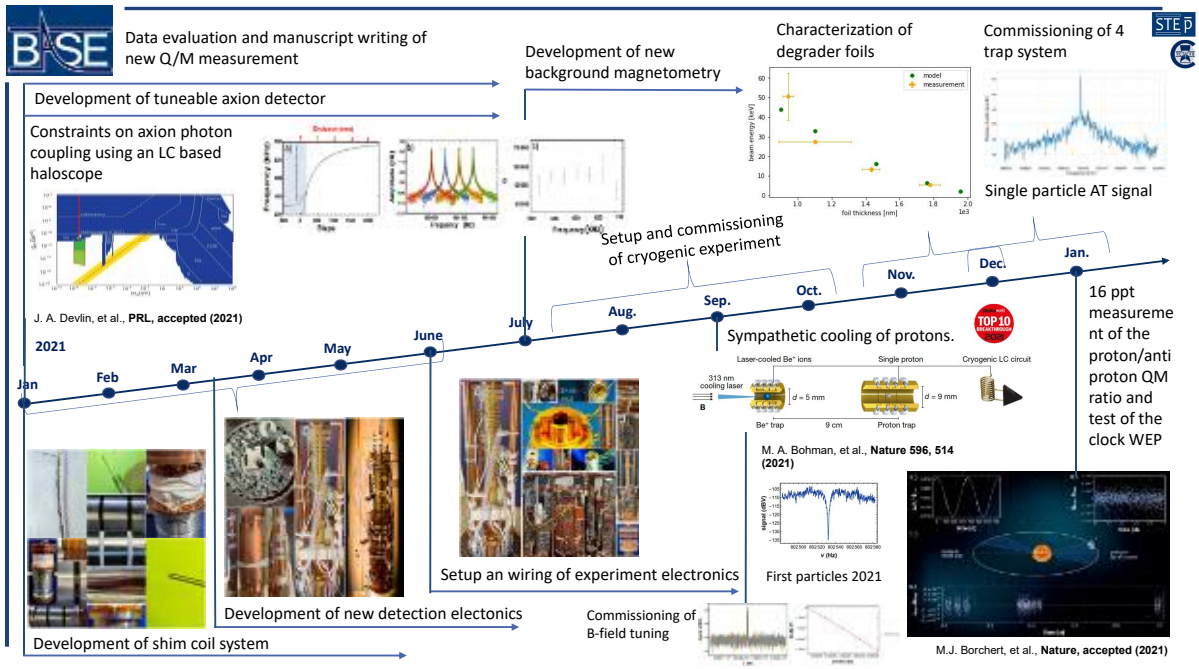

Figure 1: Graphical summary of BASE's achievements in 2021. Details of the individual aspects will be described in the report.

In addition to these main efforts, a part of the team was working on the development of the new axion haloscope BASE-CDM. Within these efforts, a high-Q highly sensitive superconducting detection system was developed, with a frequency tuneability of $> 300\,\mathrm{kHz}$. This device will increase the sensitive detection bandwidth for LC-based axion searches by more than 3 orders of magnitude, compared to [1]. We also summarize progress made at the BASE-Mainz experiment, where the first implementation of sympathetic cooling of protons by coupling the particles to laser-cooled $^9\mathrm{Be}^+$ ions was successfully demonstrated. Related work was published in Nature [2] and was selected, together with work performed by the ALPHA collaboration, as one of the top 10 physics breakthroughs of 2021 by "Physics World".

We start this report with summarizing comments on the recently published 16-parts-per-trillion measurement of the proton-to-antiproton charge-to-mass ratio [3], which also includes a stringent test of the clock weak equivalence principle. We continue with a progress update on the development of the transportable trap BASE-STEP, and thereafter describe our efforts to develop the axion haloscope BASE-CDM. Next, we describe experimental upgrades implemented for the 2021 antiproton run and detail their characterization. We conclude with summaries on the sympathetic cooling efforts carried out at BASE-Mainz and BASE-Hannover.

3 Final Data Evaluation of the Charge-to-Mass Ratio Measurement Campaign Acquired in the Antiproton Runs of 2017 to 2019

3.1 Summary

The implementation of the experiment scheme to measure the proton/antiproton charge-to-mass ratio, and the applied data analysis methods were described in detail in the last annual report. This includes a description of the experimental implementation of the measurement scheme, a description of the frequency evaluation and the used data cleaning filters, the description of weighted frequency ratio analysis and polynomial frequency ratio analysis, and a detailed analysis of systematic frequency shifts in the measurements. The contributions are discussed for both peak-based frequency measurements where the particle's modified cyclotron motion is excited, as well as dip-based frequency measurements, which take place with the particle in thermal equilibrium with the axial detection system. A condensed form of this analysis, together with updated numbers is summarized in the supplementary material of the published manuscript [3], which is also attached to this summary report. Compared to the measurement carried out in 2014 [6], the experiment stability for the recent measurement was considerably improved by implementing the following upgrades:

- A multi-layer self-shielding coil system for efficient shielding of background magnetic field fluctuations. The system, carefully described and characterized in [23], builds upon an idea introduced by Gabrielse [26]. This multi-layer shielding system suppresses certain external magnetic field disturbances by up to a factor of $S \approx 225(15)$. The self-shielding factor used in the previous BASE charge-to-mass ratio run was $S \approx 10$.
- Temperature shielding was installed, this includes shielding of the sensitive tops of the experiment cryostats, covering the previously open experiment zone by a tent, and insulating the boil-off lines connected to the helium recovery manifold of CERN with several layers of insulating foam. Compared to the 2014 charge-to-mass ratio run the temperature fluctuation of the system per frequency measurement were suppressed by up to a factor of 11.
- A very important upgrade that has been developed is a frequency-tuneable axial frequency detection system, inspired by the work described in [27]. The frequency tuneability of the system covers the antiproton-to-H^- axial frequency difference of ≈ 348.5 Hz. This system enables us to operate the trap at constant trapping voltage, which eliminates the dominant systematic error of the previous BASE charge-to-mass ratio measurement [6].
- A new voltage supply UM1-14-LN-25 which has been developed according to the specifications of BASE has been implemented. Compared to the previously used devices, the new version has a five-fold reduced output relaxation time constant (4 s).
- For the axial frequency measurement system, a single sideband downconverter (SSB) has been implemented. This improves the dip signal-to-noise ratio (SNR) by 3 dB, and enables measurements at improved frequency resolution.
- The internal reference clock of the FFT analyzer has been replaced by an external 10 MHz rubidium reference oscillator.

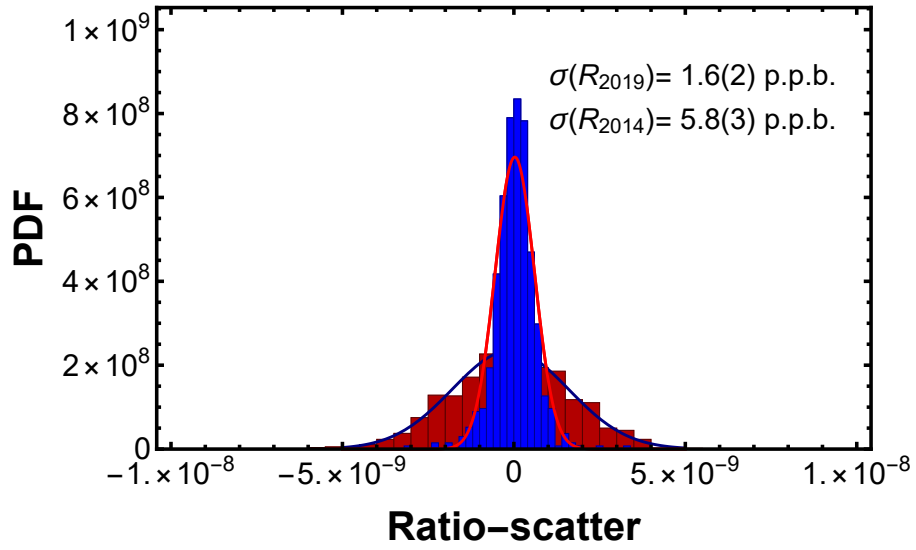

Figure 2: Comparison of experiment stability. The red histogram represents the stability of the apparatus which was used in the 2014 antiproton-to-proton charge-to-mass ratio measurement campaign [6], the blue histogram shows the stability reached with the improvements described in the text. We reach the principal limit of the sideband measurement method.

In addition to these improvements, an upgraded data logging system was installed which monitors the experiment zone temperature with multiple sensors placed in the experiment zone and on the experiment stages, and which logs the pressures of the experiment zone and the LHe atmosphere of the superconducting magnet and the cryostats. The system also contains a set of Hall sensors, GMR sensors, and several flux-gate sensors which are placed in the experiment zone. In addition, the cryomechanical support of the experiment was upgraded, and an additional protection layer around the most sensitive parts of the experiment was installed. The integrated effect of all these improvements on the experiment stability is illustrated in Figure 2. The red histogram shows the antiproton-to-H^- cyclotron frequency scatter $\sigma(\nu_{c,k+1}/\nu_{c,k})$ of the 2014 measurement campaign compared to the measurement campaign presented here (blue histogram). The dominant contribution which led to this factor of > 3 improvement is attributed to the installation of the upgraded cryomechanical support, the implementation of temperature shielding, as well as the installation of the multi-layer self-shielding solenoid system [23].

3.2 Statistical Data Analysis and Result

The data-set which is considered consists of 24 187 individual frequency ratio measurements acquired within four measurement campaigns between December 2017 and May 2019. It subdivides into two sideband measurement sequences recorded in the time-windows 12/2017 to 02/2018 (2018-1-SB), and 04/2018 to 05/2018 (2018-2-SB). After a mechanical revision of the apparatus a peak campaign was recorded in the time window 11/2018 to 01/2019 (2018-3-PK), the entire series of measurements was completed with another sideband-run taken in 04/2019 to 06/2019 (2019-1-SB). Table 1 gives an overview on the data-runs considered in the manuscript. Processing the acquired data using the data evaluation approaches described in the last annual report, we obtain the results of the frequency ratio measurements summarized in Table 2. Between the 2018 sideband runs and the 2019 sideband run, the experiment stability was improved by rebuilding the cryogenic support structure of the experiment. The peak method, also performed with the rebuilt instrument, has an intrinsically lower frequency-determination-scatter than the sideband technique.

Run	Datapoints	Period
2018-1-SB	9941	2017/12 - 2018/02
2018-2-SB	3557	2018/04 - 2018/05
2018-3-PK	2583	2018/11 - 2019/01
2019-1-SB	8106	2019/04 - 2019/06
Total	24187	2017/12 - 2019/06

Table 1: Summary of datapoints accumulated during the experiment runs entering the antiproton-to-H^- cyclotron frequency ratio presented in the main text.

Campaign	R_{exp}	$\sigma(R)_{\text{stat}}$	$\sigma(R)_{\text{sys}}$
2018-1-SB	1.001 089 218 748	$27 \cdot 10^{-12}$	$26 \cdot 10^{-12}$
2018-2-SB	1.001 089 218 727	$47 \cdot 10^{-12}$	$49 \cdot 10^{-12}$
2018-3-PK	1.001 089 218 748	$19 \cdot 10^{-12}$	$14 \cdot 10^{-12}$
2019-1-SB	1.001 089 218 781	$19 \cdot 10^{-12}$	$23 \cdot 10^{-12}$

Table 2: Results of the four antiproton-to-H^- measurement campaigns. The second column displays the measured result, the last two columns indicate the statistical uncertainty and the systematic uncertainty of the measurement.

3.3 Systematic Frequency Shifts of the Different Measurement Campaigns

The dominant systematic uncertainty of the sideband campaigns arises from a weak scaling of the measured axial frequency ν_z as a function of its detuning $\Delta\nu_z$ with respect to the resonance frequency ν_R of the detection resonator [3]. With $\Delta_z = \nu_z - \nu_R$ we determine the function $\nu_z(\Delta_z)$ based on differential measurements, and extrapolate the result to $\nu_z(\Delta_z = 0)$. The leading systematic uncertainty of the peak measurement campaign is due to resolution limits in the determination of the axial temperature of the particles $T_{z,\bar{\text{p}}}$ and T_{z,H^-}, respectively. Together with the residual magnetic-bottle inhomogeneity B_2 of the trap, a temperature difference $\Delta T_z = T_{z,\bar{\text{p}}} - T_{z,\text{H}^-}$ would impose a systematic frequency ratio shift of $\Delta R/R = -70.02\,\text{p.p.t.}/\text{K}$ and $\Delta R/R = -23.44\,\text{p.p.t.}/\text{K}$, for the 2018 sideband runs and the 2018/2019 peak and sideband runs, respectively. For all individual measurement campaigns we determine ΔT_z using different methods, and correct the measured result accordingly, details were described in the annual report of 2020 and the supplementary material of the manuscript.

Table 3 summarizes all the systematic frequency ratio shifts for all the individual measurement campaigns that were considered. The first 7 rows are due to trap imperfections and non-vanishing energy. The next six rows are related to technical shifts. The last five entries only occur in the peak based measurement and are related to unequal averaging in axial and cyclotron frequency measurements and coefficient shifts due to residual non-linear contributions in the $\nu_+(\nu_z)$ scaling that was used in the measurement.

3.4 Final Result

We have applied two different measurement methods to determine the proton-to-antiproton charge-to-mass ratio, with a fractional precision of 16 parts in a trillion. Four measurement campaigns were conducted, three of them apply the sideband method [6], one uses a peak method relying on direct measurement of the modified cyclotron frequency ν_+ with an image current detector [12]. The dominant trap-specific limitation arises from an interplay of axial temperature uncertainty and the residual magnetic bottle of the trap. The dominant systematic limitation of the sideband method comes from a characterized axial frequency shift as a function of $\nu_z - \nu_{\text{R}}$. As shown in Figure 3, which summarizes the systematic

Effect	2018-1-SB	2018-2-SB	2018-3-PK	2019-1-SB
B_1-shift	0.03(2)	0.01(2)	$<(0.01)$	$<(0.01)$
B_2-shift	20.27(14.86)	8.38(14.86)	10.79(12.66)	3.75 (5.16)
C_4-shift	(1.12)	(1.13)	(1.54)	(0.76)
C_6-shift	$<(0.01)$	$<(0.01)$	$<(0.01)$	$<(0.01)$
Relativistic	1.20(92)	0.47(90)	1.90(2.32)	0.65(94)
Image charge shift	0.05(0)	0.05(0)	0.05(0)	0.05(0)
Trap misalignment	0.06(0)	0.06(0)	0.05(0)	0.05(0)
Voltage Drifts	$-3.35(5.12)$	$-3.77(5.12)$	$-0.11(11)$	$-5.03(5.12)$
Spectrum Shift	0.37(20.65)	16.89(46.49)	0.74(61)	$-8.61(21.45)$
FFT-Distortions	(1.57)	(3.48)	(0.03)	(1.23)
Resonator-Shape	0.02(3)	0.02(2)	$<(0.01)$	0.01(2)
B_1-drift offset	$<(0.11)$	$<(0.11)$	$<(0.04)$	$<(0.04)$
Resonator Tuning	$<(0.16)$	$<(0.16)$	$<(0.06)$	$<(0.06)$
Averaging Time	–	–	$-2.87(25)$	–
FFT Clock	–	–	(3.69)	–
Pulling Shift	–	–	2.86(24)	–
Linear Coefficient Shift	–	–	0.16(40)	–
Nonlinear Shift	–	–	0.03(2)	–
Systematic Shift	18.65(26.04)	22.11(49.22)	13.60(13.50)	$-9.13(22.71)$
$R_{\text{exp}} - R_{\text{theo}}$	13.02(27.12)	$-5.04(46.57)$	7.99(18.57)	18.34(18.89)
$R_{\text{exp,c}} - R_{\text{theo}}$	$-5.63(37.60)$	$-27.15(67.76)$	$-5.61(22.66)$	27.47(29.54)

Table 3: Summary of systematic shifts and uncertainties for the sideband (SB) and peak (PK) campaigns. The peak measurement method suppresses the dominant systematic contribution of the SB method by a factor of ν_z/ν_+. Table entries are in p.p.t. units.

uncertainties of the two applied methods, this dominant limitation is suppressed in the peak method by a factor of ν_z/ν_+. Combining all the sideband measurement campaigns we obtain

$$R_{\bar{\text{p}},\text{H, SB}} = 1.001\,089\,218\,764(15)_{\text{stat}}(16)_{\text{sys}}, \tag{1}$$

the result of the peak ratio measurement is

$$R_{\bar{\text{p}},\text{H, PK}} = 1.001\,089\,218\,748(19)_{\text{stat}}(14)_{\text{sys}}. \tag{2}$$

Considering error correlation and calculating the weighted mean of the two different methods, we obtain the final result

$$R_{\bar{\text{p}},\text{H, exp}} = 1.001\,089\,218\,757(16), \tag{3}$$

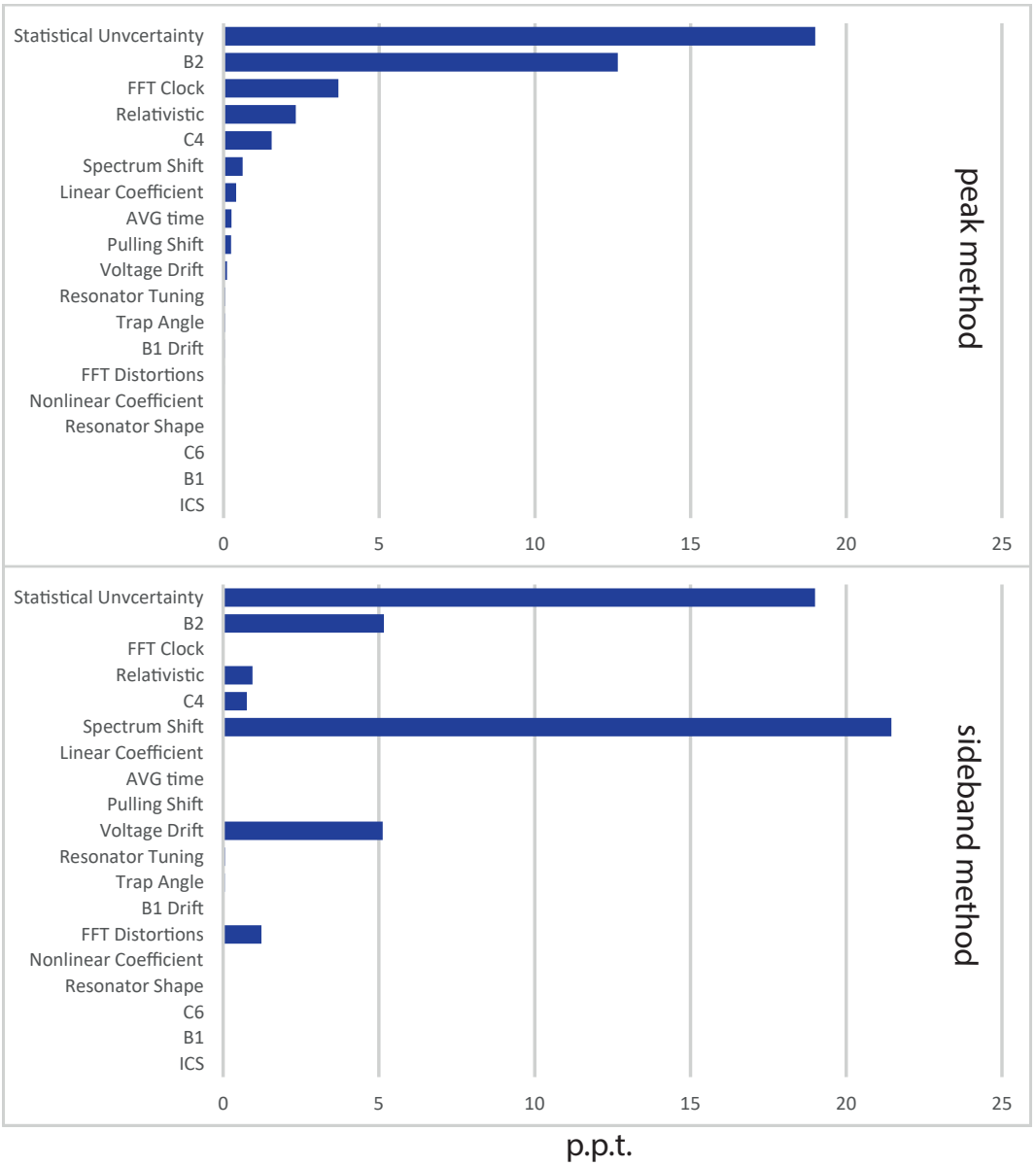

Figure 3: Top: summary of systematic uncertainties of the 2018-1-PK measurement campaign. Bottom: summary of systematic uncertainties of the 2019-1-SB measurement campaign.

corresponding to an antiproton-to-proton charge-to-mass ratio of

$$R_{\bar{\mathrm{p}},\mathrm{p},\,\mathrm{exp}} = -1.000\,000\,000\,003(16). \tag{4}$$

The result has an experimental uncertainty of 16 p.p.t. (C.L. 0.68), supporting CPT invariance. It improves our previous measurement [6] by a factor of 4.3 and upon earlier results [28] by a factor of 5.6. This measurement constitutes the most precise test of CPT invariance with baryons, and is one of the most precise mass measurements ever performed [29].

3.5 Discussion of the Result

In an illustrative model, that can however not be trivially incorporated into relativistic quantum field theory [30], Hughes and Holzscheiter have shown [31] that if there was a scalar- or tensor-like gravitational

coupling to the energy of antimatter that violates the Weak Equivalence Principle (or more specifically the universality of clocks, referred to as WEP$_c$) [32], there will be, at the same height in a gravitational field, a frequency difference

$$\frac{\nu_{c,\bar{p}} - \nu_{c,p}}{\nu_{c,avg}} = \frac{3\Phi}{c^2}(\alpha_g - 1) \tag{5}$$

between a proton cyclotron-clock at $\nu_{c,p}$ and its CPT conjugate antiproton clock at $\nu_{c,\bar{p}}$. Here $\alpha_g - 1$ is a parameter characterizing the strength of the potential WEP$_c$ violation and Φ the gravitational potential. Together with the gravitational potential of the local supergalactic cluster ($\Phi/c^2 = (G\,M)/(rc^2) = 2.99 \times 10^{-5}$) [33, 34], the measurement reported here constrains those WEP$_c$ violating gravitational anomalies to a level of $|\alpha_g - 1| < 1.8 \times 10^{-7}$, improving the previous best limits by about a factor of 4. This approach has been discussed controversially [35], since the imposed clock shift depends on the absolute value of the gravitational potential, and a WEP-violating force might have a finite range which would modify the chosen potential. This inspires the following analysis: We use the change $d\Phi_E$ of the

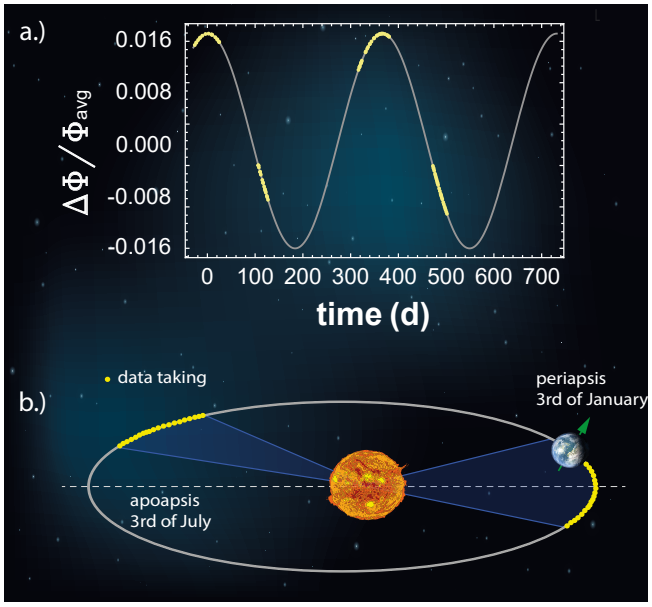

Figure 4: Trajectory of the Earth on its orbit around the Sun. a.) Variation of the gravitational potential in the BASE laboratory sourced by the elliptical orbit of the Earth around the Sun. The yellow scatter points represent the data-taking windows. b.) Scaled orbit, the blue shaded areas indicate the trajectorial fraction covered by the measurements reported here.

mean gravitational potential $\Phi_{E,avg}$ at the location of our experiment, which is sourced by the Earth's elliptic orbit $O(t) = D_p \cdot (1 - \epsilon^2)/(1 + \epsilon\cos((2\pi/t_{sid})t))$ — with eccentricity $\epsilon = 0.017$ and time of the sidereal year t_{sid} — around the Sun. The eccentricity ϵ leads to a fractional peak-to-peak variation of $d\Phi_E/\Phi_{E,avg} \approx 0.03$, as shown in Figure 4. In case of WEP$_c$ violation, this would induce a cyclotron frequency ratio variation

$$\frac{\Delta R(t)}{R_{avg}} = \frac{3GM_{Sun}}{c^2}(\alpha_{g,D} - 1)\left(\frac{1}{O(t)} - \frac{1}{O(t_0)}\right), \tag{6}$$

where M_{Sun} is the mass of the Sun and G the gravitational constant. As shown in Figure 4, our data set is distributed such that we cover about 80 % of the total available peak-to-peak variation of Φ_E. We project our measured frequency ratios to one sidereal year, and look for oscillations of the measured frequency ratio, following the approach described in [36]. From this analysis, we derive the differential constraint

$|\alpha_{g,D} - 1| < 0.030$ (C.L. 0.68), setting limits similar to the initial goals of model-independent experiments testing the Weak Equivalence Principle (or more specifically the universality of free-fall, referred to as $\mathrm{WEP_{ff}}$) by dropping antihydrogen in the gravitational field of the earth [37–39].

3.6 Coefficients of the Standard Model Extension

The measurement of the antiproton-to-H^- charge-to-mass ratio with a fractional precision of 16 p.p.t. enables us to provide improved constraints on coefficients of the standard-model extension (SME) [40]. A comprehensive manuscript discusses the impact of such measurements to searches for exotic physics, and gives a clear description of the derivation of CPT violating effects that couple to antiproton-to-H^- charge-to-mass ratio comparisons [41]. From our experiment we derive the charge-to-mass ratio figure of merit

$$|\delta\omega_c^{\bar{p}} - R_{\bar{\mathrm{p}},\mathrm{p},\mathrm{exp}}\delta\omega_c^{p} - 2R_{\bar{\mathrm{p}},\mathrm{p},\mathrm{exp}}\delta\omega_c^{e^-}| < 1.96 \times 10^{-27}\,\mathrm{GeV}, \tag{7}$$

where $\frac{\delta\omega_c^w}{q_0 B}$ is a function of coefficients $\tilde{b}_w$ and $\tilde{c}_w$ that describe the strengths of feebly interacting CPT-violating background fields, coupling to particles w, the antiproton $\bar{\mathrm{p}}$, the proton p, and the electron e^-. By performing the transformation of the coefficients to the standard Sun-centered frame [40], following the theoretical outline given in [41] our measurement enables us to set improved limits on the coefficients summarized in Table 4.

Coefficient	Previous Limit	Improved Limit	Factor
$\lvert\tilde{c}_e^{XX}\rvert$	$< 3.23 \cdot 10^{-14}$	$< 7.79 \cdot 10^{-15}$	4.14
$\lvert\tilde{c}_e^{YY}\rvert$	$< 3.23 \cdot 10^{-14}$	$< 7.79 \cdot 10^{-15}$	4.14
$\lvert\tilde{c}_e^{ZZ}\rvert$	$< 2.14 \cdot 10^{-14}$	$< 4.96 \cdot 10^{-15}$	4.31
$\lvert\tilde{c}_p^{XX}\rvert, \lvert\tilde{c}_p^{*XX}\rvert$	$< 1.19 \cdot 10^{-10}$	$< 2.86 \cdot 10^{-11}$	4.14
$\lvert\tilde{c}_p^{YY}\rvert, \lvert\tilde{c}_p^{*YY}\rvert$	$< 1.19 \cdot 10^{-10}$	$< 2.86 \cdot 10^{-11}$	4.14
$\lvert\tilde{c}_p^{ZZ}\rvert, \lvert\tilde{c}_p^{*ZZ}\rvert$	$< 7.85 \cdot 10^{-11}$	$< 1.82 \cdot 10^{-11}$	4.31

Table 4: Constraints on coefficients of the standard model extension. The second column describes the previous best limit based on [28] and [6], theorized and summarized in [41]. The third column gives the improved limit based on the measurement presented here, the fourth column shows the ratio of the second and the third column. All entries are based on C.L. 0.68.

3.7 Outlook - Phase-Sensitive Frequency Measurements and Future Improvements in q/m Ratio Measurements

During the second part of the long shutdown LS2, we have successfully implemented phase-sensitive detection techniques. Using these methods we have achieved a shot-to-shot frequency resolution of 280 p.p.t., in an averaging time of 265 s per frequency measurement. By applying this method in a better-stabilized magnet, while the accelerator is in shut-down mode, we estimate that we would be able to reach in frequency ratio measurement a fractional precision of 22 p.p.t. within one day of measurement time, which is close to the fractional resolution of the recently published 16 p.p.t. comparison of the proton/antiproton charge-to-mass ratio. The measured 280 p.p.t. frequency scatter is currently limited by the stability of the superconducting magnet. A project to further stabilize the device is ongoing. Figure 5 compares the frequency resolution and stability of the phase method to the sideband method and the peak method. Table 5 summarizes the experiment stability reached in the different BASE measurement campaigns, illustrating the progress over the years.

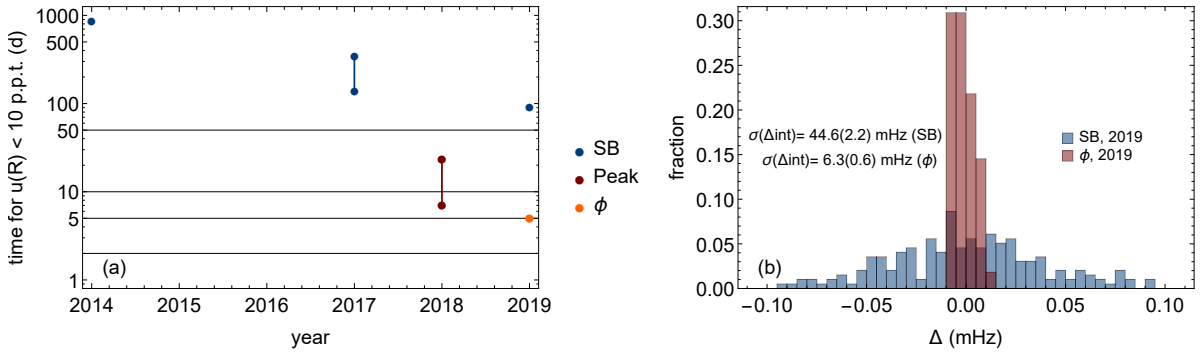

Figure 5: Left: Measurement time in days required to reach a frequency ratio resolution of 10 p.p.t. for simulated ratio measurements. Right: Comparing the cyclotron frequency scatter measured during the sideband run in 2019 (blue data) and the phase run (red data). The improvement factor is $\sigma_{\mathrm{SB}}/\sigma_{\phi} \times \sqrt{t_{\mathrm{cyc,SB}}/t_{\mathrm{cyc},\phi}} = 5$.

year	method	t_{meas}	$\sigma(\nu_+)$	$u(R)/\sqrt{t}$	$u(\nu_+)/\sqrt{t}$	$u(R)(1\,d)$
2014	SB	120 s	5.5 p.p.b.	1.45 p.p.b./$\sqrt{\mathrm{h}}$	43 mHz/$\sqrt{\mathrm{h}}$	296 p.p.t.
2017	SB (med)	120 s	2.2 p.p.b.	580 p.p.t./$\sqrt{\mathrm{h}}$	17 mHz/$\sqrt{\mathrm{h}}$	118 p.p.t.
2018	PK (med)	120 s	900 p.p.t.	240 p.p.t./$\sqrt{\mathrm{h}}$	7.1 mHz/$\sqrt{\mathrm{h}}$	49 p.p.t.
2019	SB (med)	120 s	1.8 p.p.b.	470 p.p.t./$\sqrt{\mathrm{h}}$	14.0 mHz/$\sqrt{\mathrm{h}}$	97 p.p.t.
2019	phase	265 s	280 p.p.t.	110 p.p.t./$\sqrt{\mathrm{h}}$	3.2 mHz/$\sqrt{\mathrm{h}}$	22 p.p.t.

Table 5: Antiproton-to-proton charge-to-mass ratio resolution for the frequency stability demonstrated in different experimental campaigns. The frequency scatter values $\sigma(\Delta\nu_+)$ measured during the respective runs were taken as the basis for the simulation. The frequency scatter of 280(20) p.p.t. was achieved for a magnetically calm hall. The corresponding frequency stability constitutes a stability improvement of a factor of around 13 in scatter compared to the start of BASE in 2014.

3.8 Outlook - Superconducting Shimming System

The dominant systematic frequency shift in the peak-based charge-to-mass ratio comparison — as well as in future runs to determine the proton/antiproton charge-to-mass ratio that will be based on phase methods — is due to the residual magnetic bottle B_2 in the measurement trap. The interaction of the weakly bound axial oscillator with the bottle term leads to an axial-temperature-dependent cyclotron frequency shift. At the current experimental conditions with $\Delta R/R \approx 23$ p.p.t./K, imposed by a magnetic bottle of $B_2 \approx 89\,\mathrm{mT/m^2}$, an anticipated measurement with a fractional uncertainty on the parts-per-trillion level would require a continuous axial temperature comparison with a resolution better than 0.1 K, which is difficult to achieve and will lead to considerable systematic limitations. Therefore, we follow the strategy to implement a local superconducting magnetic field shimming system as shown in Figure 6. This system consists of coils for tuning of the B_1 and B_2 magnetic field gradients. As the magnetic field gradients are also important for systematic studies in magnetic moment measurements, this system was developed in 2020, was characterized in 2021 in dedicated laboratory experiments, and is currently implemented into the new trap system. Characterization measurements that validate the successful operation of the system will be presented in Section 6.7.

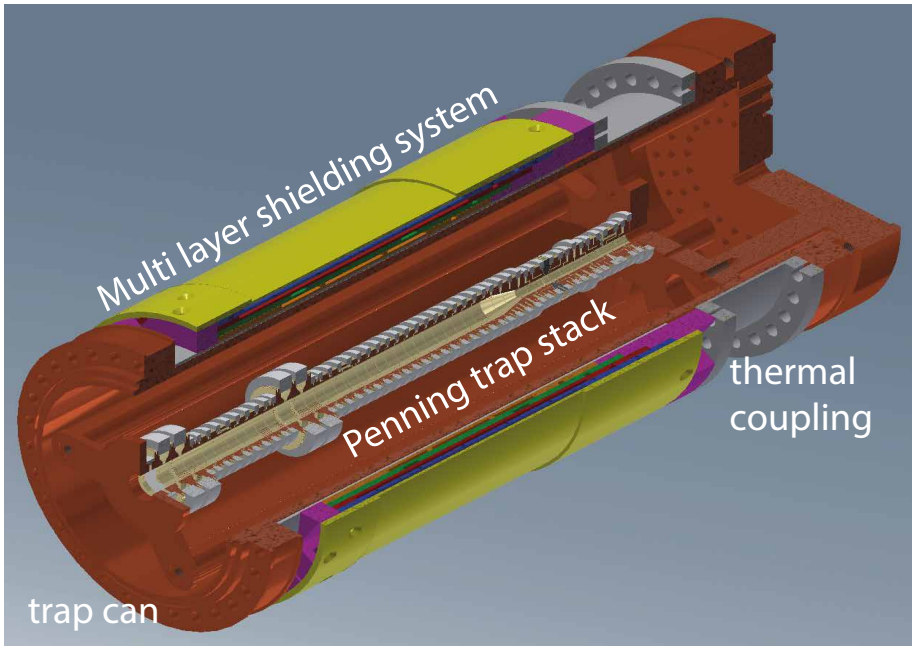

Figure 6: Technical drawing of the new trap system. Around the trap can a magnetic shimming system will be mounted which also includes a multi-layer shielding system.

4 Status and Implementation of a Transportable Antiproton Trap BASE-STEP

Another important ingredient to improve future BASE antiproton-to-proton charge-to-mass ratio comparisons is the development of the transportable antiproton trap BASE-STEP, to relocate the antiproton precision measurements from the noisy accelerator hall into a calm magnetic field environment. This will allow us to conduct our measurements entirely in offline conditions without disturbing magnetic field fluctuations from the operation of the AD/ELENA complex [25], essential to reach future improvements in comparing fundamental properties of protons and antiprotons after LS3. To facilitate independent progress on the commissioning of BASE-STEP and the antiproton precision measurements in the BASE experiment, we asked the SPSC committee for the possibility to use the former ATRAP 1 beamport to test and commission the antiproton transportable trap system. The project plans were evaluated in the last SPSC review and by the CERN research board in March 2021, and BASE-STEP was officially approved as project and for using the former ATRAP 1 experiment area.
The engineering team led by F. Butin has prepared the new experiment area for BASE-STEP, the works were finished in August 2021, and we are grateful to CERN for the support in preparing the experiment area. Next, BASE-STEP requires an additional antiproton beamline behind the vertical handover point in the experiment zone to inject the antiproton beam into the horizontal trap system. We have received support from Y. Dutheil, M. Fraser, and the ELENA team to design the beam elements and calculate the trajectories for the trap injection [42]. The additional beam transport elements are a 90 degree electrostatic deflector that was designed based on the ZDS deflectors in ELENA for lower bending angles. In addition, a focusing and steering element is needed after bending into the horizontal plane to acquire a focal point in the trap center. To this end, one ZQNA element that is used in the ELENA ejection lines was included in the beamline simulations. The production of the 90 degree deflector has been started at the mechanical workshop of MPIK. After communication with Wolfgang Bartmann, we are planning to borrow a ZQNA element from the ELENA team for the antiproton injection. This is possible once agreements on intellectual property rights have been made with the knowledge transfer department of CERN, and this would complete the set of equipment needed to inject antiprotons into BASE-STEP.
The procurement and manufacturing of the BASE-STEP trap system has been started in 2020 and is

close to being completed. The contract for the transportable superconducting magnet for BASE-STEP was signed in September 2020, and the magnet delivery is presently expected for May 2022. According to the progress report from the supplier, all hardware for the magnet is available except for the vacuum vessel and the liquid helium tank that are delayed by third-party suppliers which require up to 20 weeks of working time for such projects under the present circumstances. The experiment equipment for the BASE-STEP trap system is prepared at the University of Mainz with additional support from the Max Planck Institute for Nuclear Physics. The design of the cryogenic trap system was revised during last year and new valves were designed to reduce the residual gas flow into the antiproton storage traps and avoid the direct exposure of the antiprotons to residual gas from the injection/ejection channel. These include now commercial cryogenic piezomotor-driven rotation stages to operate the rotating electrodes. The trap system has been assembled and the wiring is almost completed. The hardware is complete except for a few components, such as a position readout for the rotating electrodes and an optimised field-emission tip for electron loading. The trap system will be equipped with four image-current detection systems, two axial detectors and two cyclotron detectors, one of each for the two traps. These four detection systems were constructed, tested and characterized in 2021 and are ready for operation.
The objectives set for 2022 are to start up the BASE-STEP trap system in the experiment area at CERN and demonstrate the transport of charged particles, ideally with antiprotons. We expect to start the installation work of experiment equipment in the BASE-STEP area as soon as travelling to CERN will not involve quarantine measures for the BASE-STEP team. With the magnet delivery scheduled for May 2022, we anticipate that we need to work two months with the magnet as preparation time before the trap system can potentially be ready for antiproton operation. In addition, we will need to install and pump the beam transport elements between the handover point and the trap system in this time window. Therefore, we expect that we can start to participate in the upcoming antiproton physics run from August 2022 , at the earliest .

5 BASE-CDM

5.1 Developments for BASE-CDM during 2021 - Tuneable Detector

In 2021 BASE demonstrated how the ultra-sensitive image current detection system [13] used to measure the antiproton's axial frequency in the spin-state analysis trap could also be used to investigate axion-like particle (ALP) dark matter [1]. There we have shown that axions that oscillate through the galaxy at their Compton frequency $\nu_a = m_a(2c^2 + \mathbf{v}\cdot\mathbf{v})/(2h)$, where $\mathbf{v}$ is the axion velocity, induce a magnetic field

$$\mathbf{B}_a = -\frac{1}{2} g_{a\gamma} r \sqrt{\rho_a \hbar c} |\mathbf{B}_e| \hat{\phi}\,, \tag{8}$$

in the toroidal image-current detector, were $\rho_a \hbar c = 4\pi^2 \nu_a^2 |a|^2/2$ is the local axion energy density, r is the radial distance from the axis of the toroid, $\hat{\phi}$ is the azimuthal unit vector, and $\mathbf{B}_e$ is the magnetic field of the BASE experiment oriented along the axis of the toroid, see Figure 7 a). The oscillating azimuthal magnetic field leads to a changing flux in the inductor, which in turn produces an oscillating voltage at the input of the first cryogenic amplification stage connected to the detector.

As illustrated in Figure 7 b), we performed a proof-of-principle measurement which was around an order of magnitude more stringent than other laboratory searches, but only for a narrow range of axion-like particle masses between 2.7906 neV and 2.7915 neV because our image current detection system could only operate at a fixed frequency. BASE's approach also incorporated a novel feature which no other axion haloscope possesses: we used a Penning-trapped antiproton to measure the detector's noise temperature. To improve our ability to search for axions in the future, we have developed a cryogenic adjustable capacitor; this allows the centre frequency of our axion detection system to be tuned over

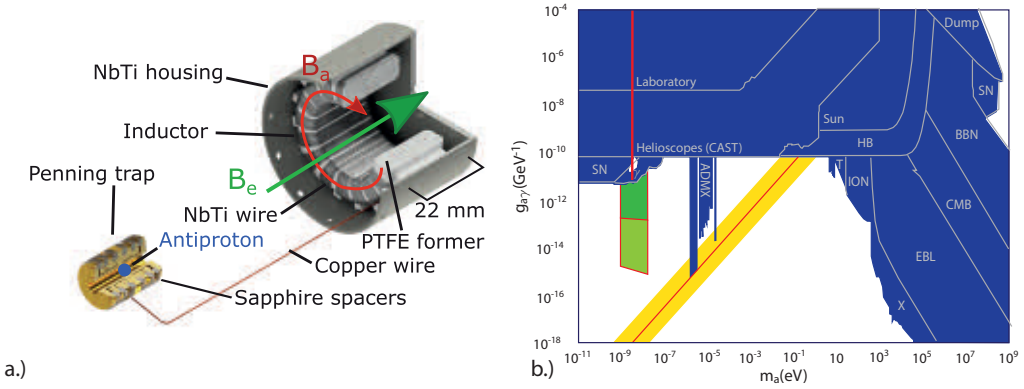

Figure 7: a.) An illustration of the main elements of the cryogenic detection system together with the external magnetic field $\mathbf{B}_e$ and the azimuthal ALP magnetic field $\mathbf{B}_a$. The NbTi end cap is not shown for clarity. b.) 95 % confidence exclusion region for the axion-photon interaction parameter as a function of the axion mass. The parameter space excluded by our analysis is shown in red, in blue the parameter space excluded by other experiments. The green region indicates the parameter space that will become accessible with the new BASE-CDM experiment dedicated to the search for axions.

one complete octave without loss of sensitivity. We constructed a small test device and validated its performance. We are also developing larger resonators which will increase our sensitivity to ALPs.

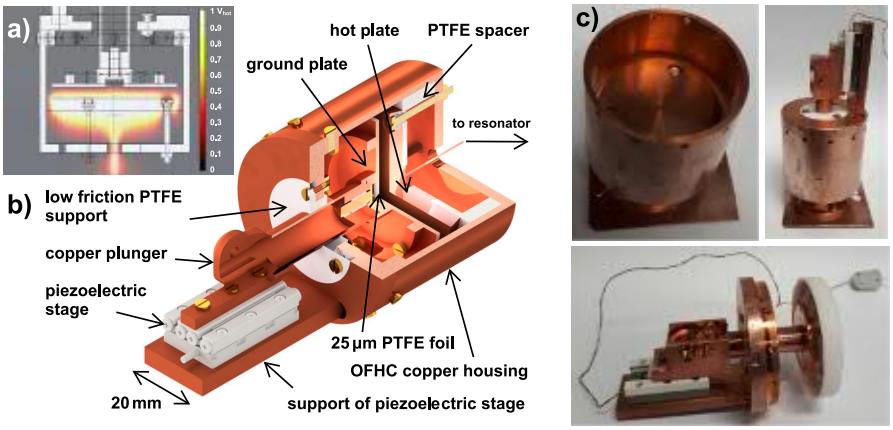

Figure 8: a) FEM simulation of the electric potential inside the capacitor. b) Cross-sectional diagram of the cryogenic adjustable capacitor. c) Photos of the capacitor. [43]

The adjustable cryogenic capacitor we constructed is illustrated in Figure 8. To minimise rf losses, we built all components from oxygen-free high conductivity (OFHC) copper and polytetrafluoroethylene (PTFE). For simplicity we chose a parallel plate geometry inside a cylindrical housing to minimise stray rf pickup. The linear motion of one plate of the capacitor is controlled by a Smaract linear slip-stick piezo drive designed to operate in high magnetic fields and under UHV conditions. This movable plate is grounded via a copper braid, and its surface is covered with a 25 µm PTFE film to prevent electrical contact. The second plate of the capacitor is connected to one end of the resonant LC detection circuit we use for axion detection. We designed the device using FEM COMSOL simulations, illustrated in Figure 8 a), to minimise the parasitic capacitance of this second plate to ground and thus maximise the scan range of the device. The measured parasitic capacitance of 11.00(55) pF is in excellent agreement with our predicted value of 11.1 pF.

To evaluate the performance of the cryogenic capacitor we connected the device to the resonant superconducting toroidal circuit which was used to set the limits in our previous axion study [1], which had an inductance L=2.73 mH and capacitance C_p=8.3 pF. A low-noise 2-stage GaAs MESFET amplifier [13] was connected to the resonant coil to read out the voltage across the resonant LC circuit. The performance of this device is illustrated in Figure 9. In Figure 9 a) we show the tuning of the resonant frequency of the detector as the movable plate is brought into contact with the fixed plate. Between 680 kHz and 425 kHz the correspondence between piezo steps and resonant frequency change agrees with our expectations for a parallel plate capacitor of these dimensions (red line). Below 425 kHz the plates come into contact with each other, and additional steps applied to the piezo motor force the plates closer together, allowing a final resonant frequency of 350 kHz to be reached. Figure 9 b) gives an illustration of successive measurements at different resonant frequencies similar to how a broadband axion search would be conducted. Finally, Figure 9 c) shows the Q-factor of the LC resonance when the amplifier is connected and the detector is connected. Over the $\sim$ 200 kHz scan range sampled, the Q-factor was at least 80 000 (almost twice as high as previously achieved) and showed no degradation.

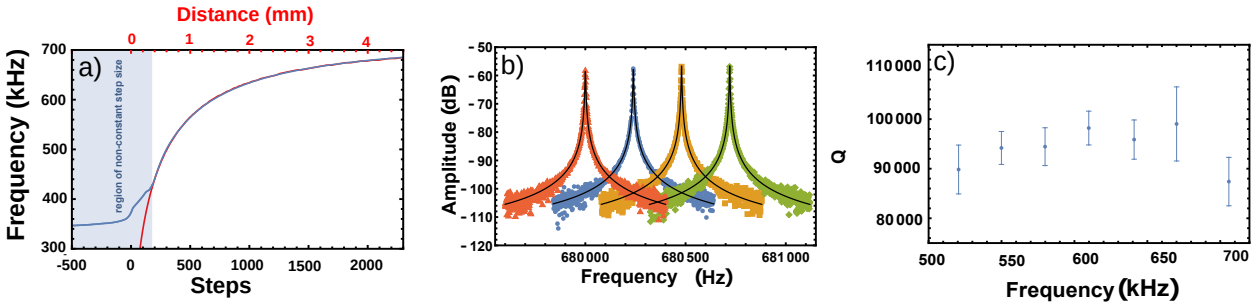

Figure 9: a) Resonance frequency of the detector as a function of steps of the piezoelectric drive with a peak to peak amplitude of 91.6 V (blue) compared to a fit based on the COMSOL simulation (red). b) Several resonator spectra at different frequencies c) Q-factor of the combined resonator, capacitor and amplifier.

With this device, we could already perform an ALP search over a 1000 times broader mass range. A more complete description of the construction and performance of this device is contained in a paper currently under preparation.

5.2 Developments for BASE-CDM during 2021 - Experiment Integration

To construct an axion detection interface with maximum possible sensitivity, considering the geometric boundary conditions of the experiment, we are currently developing the device shown on the left in Figure 10. This cryogenic inlay has the same geometry as the cryogenic part of the BASE experiment and fits into the superconducting experiment magnet. Since the sensitivity of the axion detection limits scales $\propto VB$, where V is the volume of the resonator and B the background magnetic field, this device fills the volume of the magnet bore with three RF resonators operated in different frequency ranges, one in the range of 100 kHz to 500 kHz, another one in the range 500 kHz to 1.5 MHz and a last one in a frequency range of 30 MHz to 100 MHz. It is planned to install this new device into the BASE experiment magnet during accelerator shutdown when no antiprotons are available (e.g. during LS3).

Status: The cryogenic mechanics, the central resonator and one of the small resonators have been constructed, ordered and delivered, the devices are currently being set up and tested in the BASE offline laboratory. Currently we are planning to have all the resonators operational by the end of 2022.

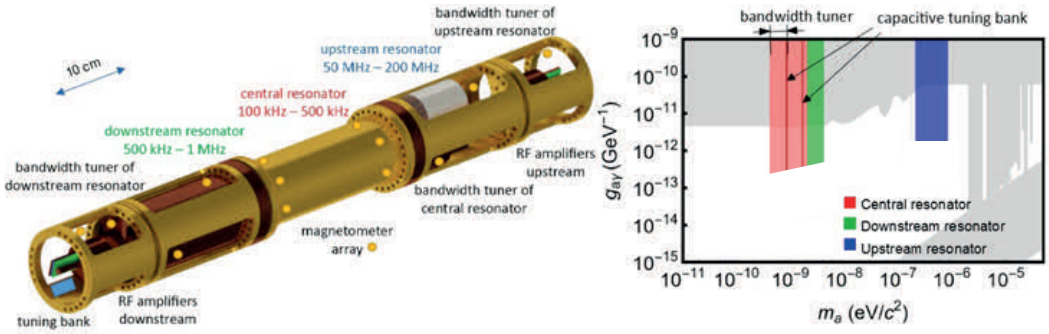

Figure 10: Left: Layout of the BASE-CDM experiment. It contains three superconducting LC resonators which fill the entire volume of the bore of the BASE magnet. Each detector will be supplied with a tuning mechanism. Cryogenic magnetometers will be placed around the entire detector setup. Right: Coupling regions and limits that can be constrained by the new experiment.

6 Towards an Improved Measurement of the Antiproton Magnetic Moment

Proton and antiproton magnetic moment measurements are among the most difficult experiments that can be carried out in Penning traps, since they require the simultaneous measurement of the spin precession frequency ν_L and the cyclotron frequency ν_c to determine the magnetic moment $g/2 = \mu_p/\mu_N = \nu_L/\nu_c$. While the measurement of the cyclotron frequency is a straight-forward technique, the determination of ν_L is a challenge. The sensitivity of the continuous Stern-Gerlach effect, which is used to get access to ν_L, scales proportional to the magnetic-moment-to-mass ratio. Compared to the electron, this ratio is more than 1 million times smaller for protons, which makes proton and antiproton spin transitions extremely difficult to observe. Given technical constraints of state-of-the-art Penning trap experiments, the detection of antiproton spin transitions requires the use of a magnetic bottle with a strength of the order of $B_2 = 100\,\mathrm{kT/m^2}$, in BASE B_2=276(8) kT/m^2 is used. At the parameters of the experiment a spin transition induces in such a B_2 an axial frequency shift of about 170 mHz out of ≈ 650 kHz. To observe these tiny frequency shifts induced by spin transitions under the extreme magnetic field conditions is challenging, since noise-driven quantum fluctuations in the radial modes induce considerable axial frequency instabilities [22]. Thankfully, the cyclotron transition rate scales with the radial quantum number of the cyclotron oscillator, such that for radially cold particles, with cyclotron energies of the order 10 µeV, high-fidelity spin transition detection can be achieved [8, 16]. To achieve such low radial particle temperatures, a method called sub-thermal cooling is used. This method, however, is time consuming to apply. Another disadvantage of the strong magnetic bottle is the fact that it leads to broadening of the Larmor resonance line, which limits single trap magnetic moment measurements to the parts-per-million level [15]. To overcome these limitations and inspired by ideas of Haeffner and collaborators [44], we have invented a two-particle/three-trap technique, which enables magnetic moment determinations with parts-per-billion precision [19].

This method is based on a "precision trap" with a homogeneous magnetic field, an "analysis trap" with the superimposed magnetic bottle, and a "park trap" adjacent to the precision trap. Two particles are loaded into this trap stack, a hot "cyclotron" antiproton for measurements of ν_c in the precision trap and a cold "Larmor" antiproton for spin flip experiments in the precision trap and spin state detection in the analysis trap. To acquire data points, the experiment would start with the preparation of an antiproton with single spin flip fidelity in the analysis trap, and another antiproton in the precision trap. Afterwards we

- identify the spin state of the Larmor particle in the analysis trap.
- Measure the cyclotron frequency with the cyclotron particle in the precision trap.

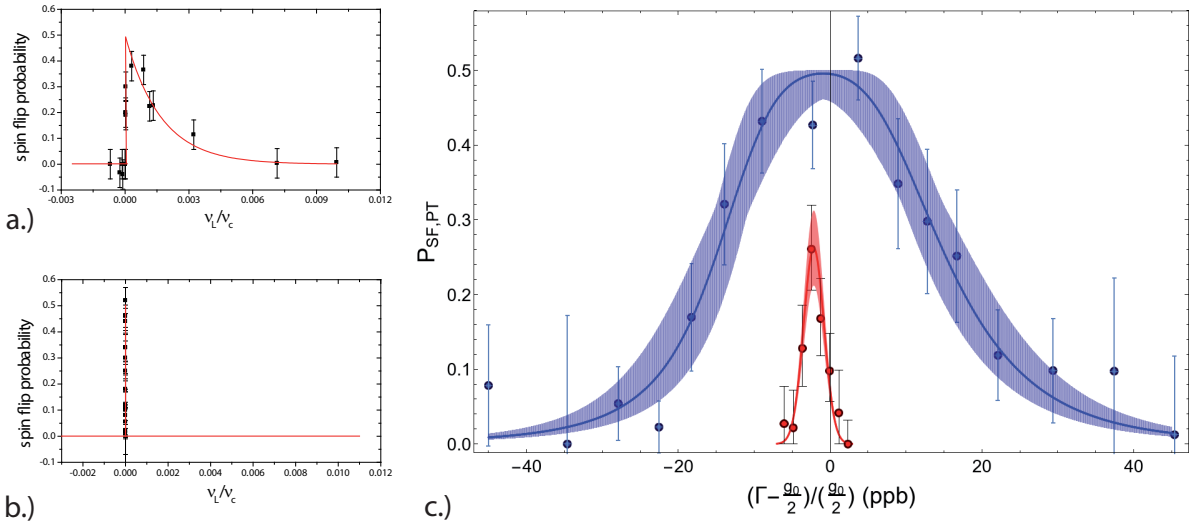

Figure 11: Antiproton g-factor resonances measured by BASE. a.) 2016 g-factor resonance measured in the BASE analysis trap with its strong superimposed magnetic bottle. b.) g-factor resonance measured with the two-particle/three-trap method plotted on the same scale as a.). c.) zoomed version of the antiproton (blue) g-factor resonance shown in b.) and proton (red) g-factor resonance measured in 2016/2017 at BASE-Mainz.

- Move the cyclotron particle out of the precision trap to the park trap, and the Larmor particle from analysis trap to the precision trap, and induce a spin transition.
- Move the particle configuration back to the initial state, measure ν_c with the cyclotron particle in the precision trap and analyze afterwards the spin state of the Larmor particle in the analysis trap.

This scheme measures the magnetic moment of the particle in the homogeneous magnetic field of the precision trap, compared to measurements in the inhomogeneous analysis trap this narrows down the spin-flip resonance by more than a factor of 1000, as shown in Figure 11. The successful implementation of this method enabled us to determine the antiproton magnetic moment to

$$\frac{\mu_{\bar{\mathrm{p}}}}{\mu_{\mathrm{N}}} = -2.792\,847\,3443(46) \tag{9}$$

which has a fractional precision of 1.7 p.p.b., and improves the previous best measurement carried out by the ATRAP collaboration [14] by more than a factor of 3000. Measurements carried out in parallel at the BASE-Mainz experiment [21] determine the proton magnetic moment to

$$\frac{\mu_{\mathrm{p}}}{\mu_{\mathrm{N}}} = 2.792\,847\,344\,62(82). \tag{10}$$

This improved our previous best measurement by a factor of 11 and the precision of results carried out with hydrogen masers in magnetic fields by a factor of 33. These two antiproton and proton magnetic moment measurements can be combined to

$$\left(\frac{\mu_{\mathrm{p}}}{\mu_{\mathrm{N}}} + \frac{\mu_{\bar{\mathrm{p}}}}{\mu_{\mathrm{N}}}\right) = 0.3(8.3) \times 10^{-9}, \tag{11}$$

the uncertainty in brackets represents the 95 % confidence interval.

The next antiproton runs will be dedicated to the goal to perform an improved measurement of the

antiproton magnetic moment, compared to [19] with at least 5-fold improved fractional precision. The new experiment includes

- new detection systems for cyclotron frequency measurements,
- new filter electronics to further suppress heating rates in the analysis trap,
- the superconducting coil system already mentioned above,
- a cooling trap for efficient sub-thermal cooling cycles to prepare antiprotons with high spin state detection fidelity.

In addition CERN has upgraded the AD antiproton physics program from the previously used antiproton decelerator, which provided antiprotons at an energy of $5.3\,\mathrm{MeV}$, to the ELENA synchrotron, which delivers antiprotons at $100\,\mathrm{keV}$. **This required a considerable experiment upgrade to replace the previously used 25 µm stainless steel degrader foil to a degrader with a thickness matched to the 100 keV ELENA antiproton energies, while maintaining the challenging vacuum requirements of BASE.** In addition to these major upgrades, the superconducting detection systems for all four traps, reservoir trap, precision trap, analysis trap and cooling trap were upgraded and improved.

6.1 Revised Electronics Setup

Penning trap measurements rely on measurements of the motional frequencies that are defined not only by the strong, homogeneous magnetic field, but likewise by the DC voltages which are applied to the cylindrical trap electrodes. As a direct consequence, highly stable trap conditions with highly stable motional frequencies and low heating rates require sufficiently stable voltage sources and heavy filtering to suppress residual voltage noise. We employ commercial power supplies with sub-p.p.m. stability on the time scale of a day in combination with up to four RC-filter stages for each trap electrode for this purpose. Endcap and transport electrodes are switched to ground potential during precision measurements. RF lines for particle excitation are shielded and connected to their electrodes through capacitive attenuators. For the 2021 run we redesigned most parts of the electronics setup at both cryogenic and room temperature stages.

6.1.1 DC biasing

The DC bias voltages are provided by commercial power supplies (Stahl Electronics – UM-1-14) and filtered at room temperature, $77\,\mathrm{K}$, and twice at $4\,\mathrm{K}$. Based on experiences from our earlier runs, this filtering concept has been completely revised, refined, and rebuilt. All filters use two parallel resistors of $1\,\mathrm{M\Omega}$ combined with a $10\,\mathrm{nF}$ capacitor yielding a cutoff frequency of about $30\,\mathrm{Hz}$. This is sufficiently high to allow for adiabatic particle transport with slow voltage ramps on the $100\,\mathrm{ms}$ time scale. An exemption is made for the two high-voltage lines which are directly connected to two capture electrodes and allow for fast switching and thereby the capture of antiprotons from the ELENA beamline. However, these capture electrodes are sufficiently far away from the relevant Penning traps for precision measurements.

6.1.2 RF lines

The wiring concept has to deal with two different RF lines: excitation lines to manipulate the motional amplitudes of the trapped particles and signal lines which connect image-current pick-up electrodes to

particle detectors, namely cyclotron detectors which operate at about 30 MHz and axial detectors operating between 600 and 800 kHz. These signal lines are bare 1 mm OFHC copper wires without any coaxial shield to avoid any additional parasitic capacitance. The cyclotron detectors are operated inside the trap can to keep the signal lines as short as possible and to avoid the usage of vacuum feedthroughs, which again would affect the detection performance significantly owing to their compromising RF properties. The axial detectors are placed outside the trap can, inside a dedicated electronics segment and connected to their respective pick-up electrodes via special Sapphire isolated feedthroughs which have better RF properties than the PTFE isolated feedthroughs used in pure bias lines. The excitation lines, by contrast, are coaxial lines with capacitive attenuators and high impedance RF-blocks on the 4 K stage that protect the DC voltage sources.
Additionally, we implemented cryogenic filters for all excitation lines related to the analysis trap, as any noise can potentially disturb the spin flip measurement. Two of them are also switched to physical ground using cryogenic switches.

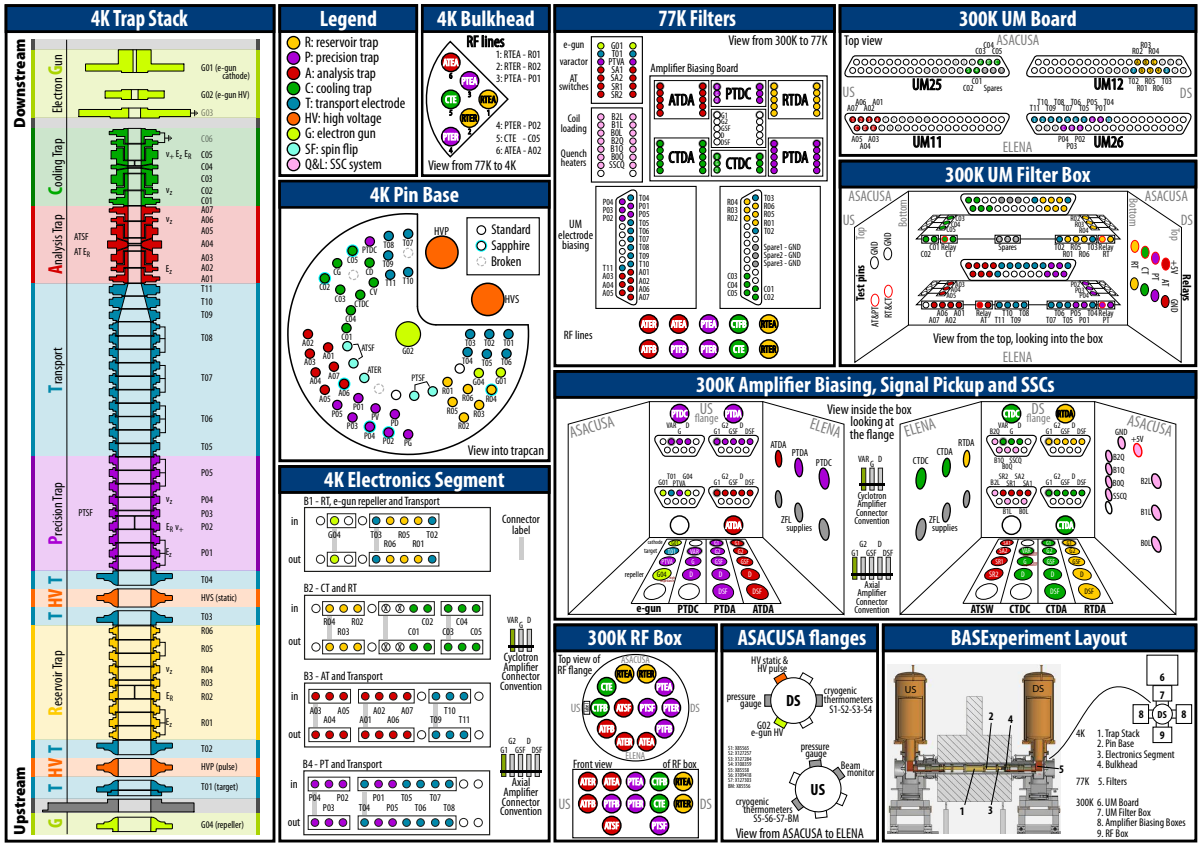

Figure 12: Electronics scheme of the BASE experiment. Most of the boards were redesigned during the long shutdown in 2020/2021.

6.2 Development of a New Degrader System to Interface BASE to ELENA

6.2.1 Introduction

In previous years the antiproton beam was provided by the Antiproton Decelerator, which delivered particles at an energy of 5.3 MeV. Since 2021 the antiproton beam is provided by ELENA with an energy of only 100 keV. This requires a degrader with a thickness of about 1-2 µm, depending on the material of the window. In this section, we present the status of the design and tests of the new, micrometer

foil	K_{foil} [m^2/s]
2.5 µm Mylar	1×10^{-12}
2 µm Mylar + 80 nm Al	4×10^{-14}
2 µm Mylar + 80 nm Al on both sides	1×10^{-14}

Table 6: Permeation constant of the Mylar foil without and with one or both sides aluminised with 80 nm thick layer, measured for a 1.2 mm diameter hole.

thick, tight vacuum window, which allows for efficient antiproton deceleration and long-time storage of antiprotons in the Penning Trap system of our experiment.

6.2.2 Design of an Ultra Thin Cryogenic Vacuum Window

One of the unique features of the BASE trapping system is the ability to store antiprotons for many years [17]. One of the main challenges is to reach pressures lower than 7×10^{-17} mbar to avoid annihilation of antiprotons with residual gas. Such low pressures are achieved by first baking the system to ≈393 K and pumping it to $\approx 10^{-7}$ mbar pressure. Afterwards, the indium sealed trap chamber is permanently closed with a pinch-off technique and subsequently cooled to 4 K. The adsorption of the residual gas on the walls of the experiment at cryogenic temperatures allows us to reach partial pressures of residual helium and hydrogen below $p_{He} < 1.04 \cdot 10^{-19}$ mbar and $p_H < 0.46 \cdot 10^{-19}$ mbar, where the upper limits are obtained from the storage time of the antiprotons in the trap [45]. Keeping such low vacuum levels for a year requires excellent separation of the trap chamber from the surrounding insulation vacuum with a tight vacuum window. Ideally, to efficiently perform experiments, this window should also act as a degrader, which decreases the energy of the antiproton beam to 1 to 5 keV allowing for efficient trapping. However, as already mentioned, due to the very low energy of the incoming antiproton beam from ELENA, the vacuum window needs to have a thickness between 1 and 2 μm. The combination of the strict vacuum requirements and the maximum allowed thickness constraints constitute a great technological challenge.

The main parameter characterising the vacuum properties of a foil of thickness d and open surface A is its leak-rate for a given pressure difference Δp and is equal to

$$L_{\text{foil}}(A, d, \Delta p) = K_{\text{foil}} \times \frac{A}{d} \times \Delta p$$

where K_{foil} is the permeation constant of the foil. Our vacuum window is based on Mylar foil, as its high endurance properties were already reported in [46, 47], and it has a low permeation constant at the level of 10^{-12} m^2/s. In the final design, the foil is aluminised on both sides with a thin layer of aluminium, which according to our measurements decreases the permeation constant of the foil by about two orders of magnitude, depending on the aluminium thickness, see Table 6 for comparison. Also, the mechanical properties of the foil, its resistance to stretching, and endurance largely increase after metallisation.

A scheme which illustrates the technical implementation of the vacuum window is shown in Figure 13. The main seal is achieved with an indium seal placed inside the groove in a specially designed degrader flange squeezed by a stamp that is tightened by a clamp. The foil which closes the window is glued to the mesh-like stamp which is covered by a thin layer of Apiezon N grease before the foil is placed on top. Then, the outer part of the foil is covered with a Kapton ring, which ensures that the foil is not destroyed by the indium seal. The degrader system is held in position by the clamp, which ensures an even pressure distribution over the entire foil surface. The size of all elements were optimised to fit into the BASE apparatus.

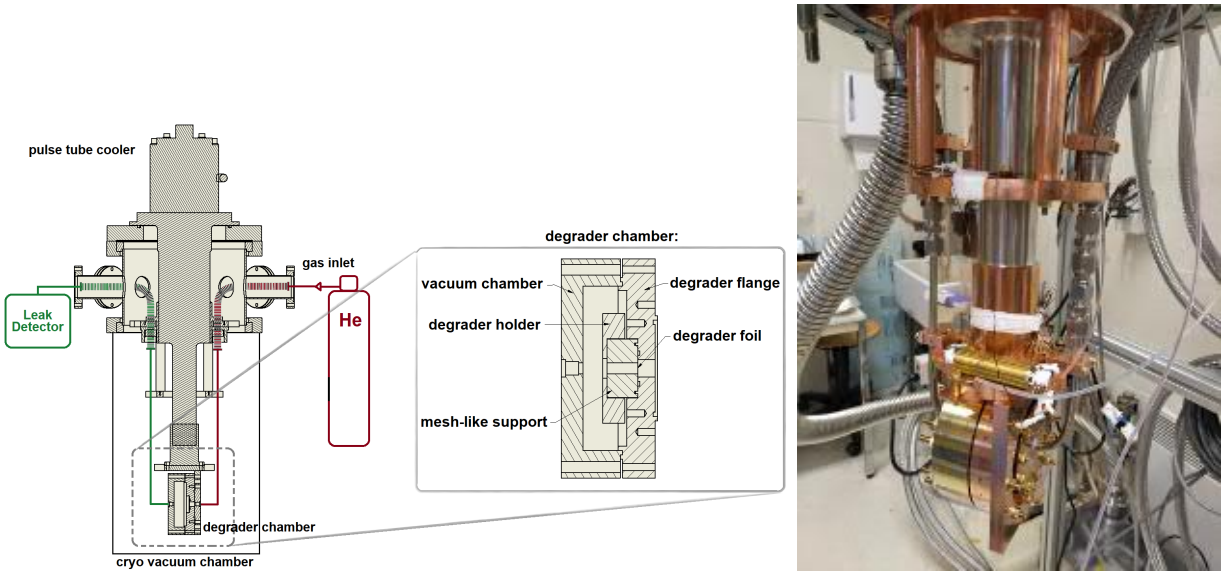

Figure 13: Scheme of the measurement system consisting of the cryocooler, leak detector, helium supply and the tested degrader system.

The surface of the window is defined by the holes in the stamp. For systematic studies we tested different hole sizes and configurations with up to 17 holes in the stamp. In the final setup which was used for the experiment operated in the 2021 antiproton run, the stamp has 7 holes with 1 mm diameter per hole, placed in the center and the corners of a regular hexagon with a side length of 1.5 mm. According to our estimations, this configuration should give 17 % geometrical acceptance for the ELENA antiproton beam.

6.2.3 Cryogenic Test Setup

To develop a vacuum-tight cryogenic window of $1 - 2$ µm thickness we performed different helium leak-rate measurements through various foils, both at room and cryogenic temperatures. The developed experimental setup is shown in Figure 13. The main part is made of OFHC copper for excellent thermal conductivity and nonmagnetic properties. The set-up consists of a degrader chamber which is cooled down to 2.7 K using a Sumitomo RDK-408D2 cryocooler. One side of the degrader chamber is pumped using a TMP built into the Leybold Phoenix L300i leak detector, which allows us to measure the leak-rate through the designed window down to the level of 1×10^{-12} mbar l/s. The other side of the degrader chamber is connected to the helium supply, which allows to reach up to 1.5 bars of He pressure. In the middle of the chamber, the designed degrader system is placed, which is the actual vacuum window. In this configuration we measured that the leak through our vacuum window with 1960 nm thick foil is at the level $< 4 \times 10^{-11}$ mbar l/s for 1 bar helium pressure difference measured at 6 K temperature. The obtained result allows us to state that the designed window should not limit the lifetime of antiprotons inside the BASE experimental chamber.

6.2.4 Measured Vacuum in the Trap Can

The new foil system was integrated into the BASE setup, as a degrader for the antiproton beam and an XHV window, see Figure 14. It was mounted inside the bore of the 1.945 T magnet as a part of the trap can, and cooled with liquid helium to 4.5 K. A copper foam absorber is added to the system to enlarge the cryopumping capacity in order to adsorb molecules later which are permeated into the trap can during

the installation process, i.e. in between the pinch-off and pumping of the insulation vacuum (pressure of about 1×10^{-8} mbar). With the designed vacuum system closed with a 1960 nm foil, we did not lose

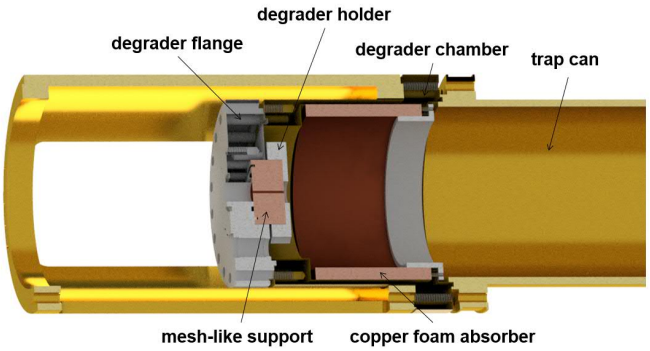

Figure 14: Scheme of the new, vacuum tight, micrometer thick degrader window implemented in the BASE experiment.

any particle since the last closure of the experiment, i.e. 90 days up to the beginning of January 2022. Under the very conservative assumption that we had only one particle in the trap, we can state that the partial pressures in our system are smaller than $p_{\mathrm{He}} < 6.0 \times 10^{-17}$ mbar and $p_{\mathrm{H}} < 2.6 \times 10^{-17}$ mbar. Also, during a short 2021 run, we tested that the vacuum window is resistant to multiple cooling and pumping cycles, which is an extremely important feature as it allows to open the outer vacuum of the BASE system without opening the trap can.

6.2.5 Degrading Properties of the Mylar Foil

In the 2021 run, we tested the degrading properties of different thicknesses of Mylar or aluminised Mylar foils in order to establish which foil thickness is the best to use in the future in BASE. For this, we performed a time-of-flight measurement of particles emitted from the degrader within a 6° angle. The transmitted particles were annihilating at least 65 cm behind the foil, which allows us to distinguish them from the annihilations inside the degrader. This is used to estimate the energy of slowed antiprotons. Tests were performed for 5 different foils: 900 nm thick pure Mylar, 900 nm Mylar with two 100 nm thick layers of Al, 1400 nm, 1700 nm, and 1900 nm foils covered with two layers of 30 nm of Al. The measured energy of the transmitted beam as a function of the foil thickness is shown in Figure 15. In the case of the 1960 nm foil, the data are hard to analyse due to lack of detection sensitivity. For that reason the blue point represents only an estimated energy based on the comparison of the data with simulations. The results are compared to an independent self-developed phenomenological model based on the stopping power data for antiprotons in carbon [48], further data taking to benchmark this model is planned in the next antiproton run.

6.2.6 2022 Setup

Based on the time of flight measurement presented in the previous section, we have decided to use a foil with a thickness 1760 nm in the next run. This will increase the expected geometrical/magnetic field/energy acceptance of the whole degrading system to 2.5 %, which is at least two orders of magnitude higher than for the 2021 setup. For this we will implement a few improvements, like a much more sophisticated antiproton beam detection system, modernised mesh-like support for the degrader foil, dynamic magnetic field shielding, and new, fast high voltage switches.

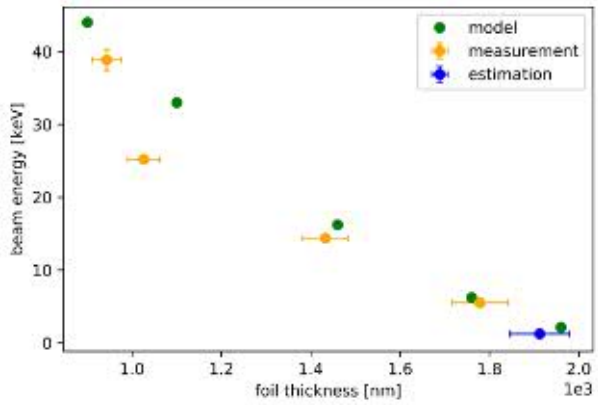

Figure 15: Measured energy of the transmitted beam as a function of the foil thickness compared to the simple phenomenological model based on measured data of the stopping power of antiprotons in carbon [48]. The 1960 nm (blue) point represents the estimated energy based on a comparison of the measured data with the simulation.

6.3 Setup for the Antiproton Run - Timeline 2021

As outlined above, the implementation of the new four trap system for the planned improved magnetic moment measurement required a considerable revision of the previous experimental apparatus. The technical implementation of all these projects kept the team busy between January 2021 and August 2021. Within this time window the mentioned components were developed and implemented. Figure 16 shows photographs of some of the developed components, the trap on the left, the superconducting shielding system in the center and cryogenic electronics and the new cyclotron detector on the right.

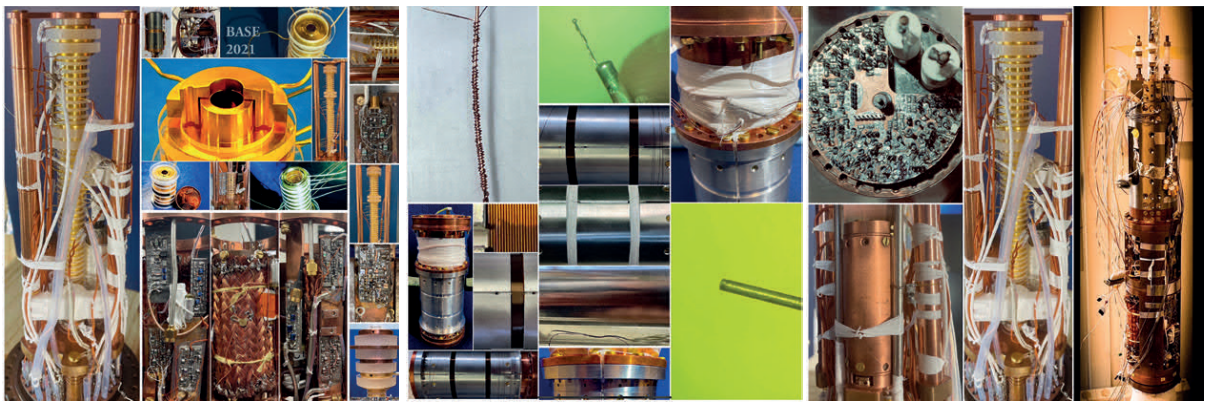

Figure 16: Images of the components newly developed for the 2021 magnetic moment run. The images on the left show the new trap systems and detection electronics, the photos in the center show elements of the superconducting shimming system, and on the right hand side cryogenic electronics, the new cyclotron detector and the assembled electronics segment are shown.

As is often the case with the development of new components for cryogenic experiments, a successful setup and commissioning usually requires several iterations. The time August 2021 to October 2021 was used for several experiment cooling cycles which were required to achieve stable experiment operation with reliably working components.

6.4 Development and Characterization of the New Cyclotron Detection Electronics for the Precision Trap

In the previous charge-to-mass ratio measurements we have used a cyclotron detection system with a quality factor of $Q = 196(8)$ operated at a resonance frequency of $\approx 29.6\,\mathrm{MHz}$. The frequency tuning range was adjusted with a varactor diode connected in parallel to the detection resonator. Due to the comparably low quality factor of the device, an excitation energy for the modified cyclotron mode of the particle of about 5 eV was required to be able to produce a visible particle signature on the detector. High excitation energies cause considerable systematic frequency shifts and frequency measurement scatter, which enters the width of the measured frequency ratios. To reduce the related undesirable effects and to be able to detect single particles at lower excitation energy, a new cyclotron detection system for the precision trap was developed, successfully implemented and characterized. Compared to the previously used system the geometry of the detection solenoid was changed and PTFE insulated 2 mm diameter annealed copper wire was used to manufacture the new pickup coil. The properties of the new detection system, when connected to the trap, are summarized in Table 7.

Table 7: Measured properties of the new PT cyclotron detector compared to the properties of the old detection system. Compared to the previously used detection system the newly developed device has a 3 times higher frequency tuning range and a 6-fold improved detection sensitivity.

Property	Value 2021	Value 2019
Resonance Frequency	29.64 MHz	29.64 MHz
Tuning range	4.3 MHz	1.5 MHz
Inductance	1.52 μH	1.68 μH
Capacitance	2.72 pF	2.63 pF
Free Q @ 5 K	1250(150)	196(8)
Detection Resistance @ 5 K	376 kΩ	61 kΩ

Connected to the experiment, the new device shows an about 6 times higher quality factor than the previously used device, which has effects on detection sensitivity and the cooling time constant to thermalize the particle, of utmost importance for spin flip experiments which require particles at low cyclotron energy prepared by sub-thermal cooling [22].
To characterize the energy resolution of the detection system, we measure the trap gradient B_1 by shifting the particle along the trap axis while measuring the modified cyclotron frequency. Subsequently we excite the particle and simultaneously measure the axial frequency ν_z and the modified cyclotron frequency ν_+. These simultaneous measurements allow us to determine the parameter B_2 and provide all parameters needed to characterize the detection sensitivity of the newly developed device. Figure 17 shows a single trapped particle with the cyclotron mode excited to an energy of $E_+ \approx 1\,\mathrm{eV}$, tuned to resonance with the cyclotron detection system. In previous experiments, energies at the level $E_+ \approx 5\,\mathrm{eV}$ were required to obtain comparable signal-to-noise ratios. A more detailed characterization of the detector is currently in progress.

6.5 Axial Detection System of the Precision Trap

The axial detection system of the precision trap is one of the most important devices in the BASE setup since it determines the properties of the particle during precision frequency measurements. Connected to the trap, the resonance frequency of the device is 649100 Hz at a quality factor of 29500 and a signal-to-noise ratio of 32 dB, corresponding to an excellent sensitivity [13]. To determine the temperature of the detector we use cyclotron excitation scatter measurements. In these experiments the particle's cyclotron mode is coupled to the axial detection system using a sideband drive. After the sideband coupling the

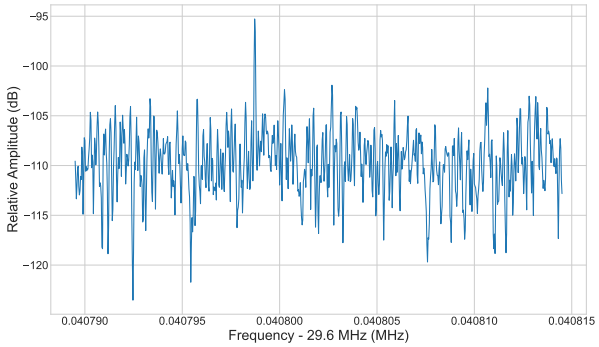

Figure 17: Single trapped particle with modified cyclotron mode excited to an energy of ≈ 1 eV. The new cyclotron detector has an about 6 times higher sensitivity than the device used in the previous charge-to-mass ratio measurement.

axial frequency $\nu_{z,0}$ is measured. Next, the modified cyclotron mode is excited with a bursted drive and the axial frequency of the excited particle $\nu_{z,e}$ is measured again. From the axial frequency shift $\Delta\nu_z = \nu_{z,e} - \nu_{z,0}$, the modified cyclotron energy E_+ can be determined. The scatter of the modified cyclotron energy after such excitation is given by

$$\sigma(E_+) \approx \sqrt{2E_{\text{th}}E_{\text{exc}}}, \tag{12}$$

where $E_{\text{th}} = k_B T_z(\nu_+/\nu_z)$ and T_z is the temperature of the axial detection system. By repeating such scatter measurements for different drive excitation energies, the temperature of the axial detection system can be extracted. Do note that the translation of measured frequency scatter $\sigma(\Delta\nu_z)$ and related energy scatter $\sigma(E_+)$ relies on the determination of the magnetic field coefficient B_2 in the precision trap [3]. From the preliminary results shown in Figure 18 a.) we obtain an axial temperature of $T_z = 11.2(7)$ K.

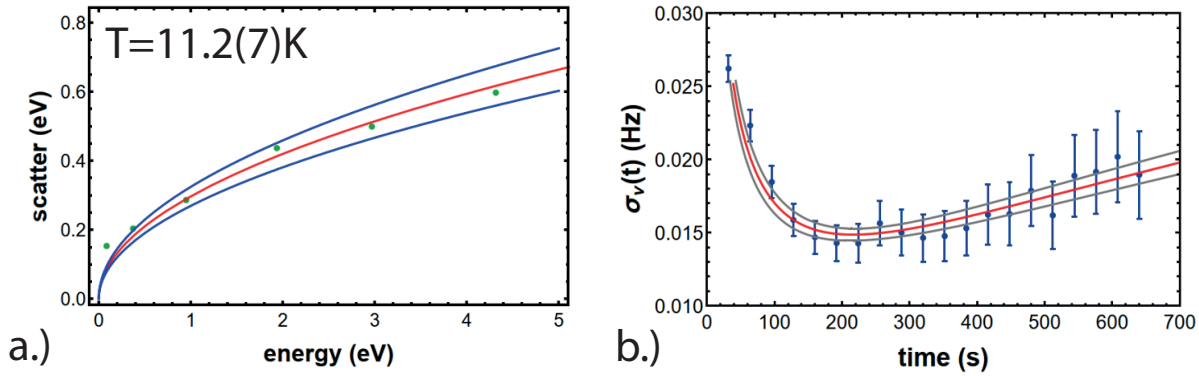

Figure 18: a.) Cyclotron excitation scatter in the precision trap as a function of the cyclotron energy, from such measurements we determine the temperature of the axial detection system. b.) Axial frequency stability in the precision trap, a higher frequency stability has not been observed in BASE before.

Another important parameter in the precision trap is the axial frequency stability as a function of averaging time. Results are shown in Fig. 18 b.). With the new setup we reach within averaging times of ≈ 30 s axial frequency fluctuations < 30 mHz. Within averaging times of ≈ 100 s a frequency scatter of ≈ 15 mHz is reached, limited by the voltage scatter of the power supply which defines the trap potential. After 200 s of averaging time we observe a slow inrease of frequency scatter, likely related to slow thermal drifts in the accelerator hall, further stabilization will be subject of the 2022 run. Nevertheless, under the current conditions the performance of the axial detection system of the precision trap is suf-

ficient to measure the antiproton magnetic moment with at least 10-fold improved precision compared to [19].

6.6 Trap Stack - Magnetic Gradients in the Precision Trap

In the new version of the BASE trap stack, and compared to the previous magnetic moment measurement [19], the distance between the analysis trap and the precision trap was increased, with the intention to reduce the magnetic field inhomogeneity in the precision trap that is imposed by the stray magnetic field of the strong magnetic bottle in the analysis trap. For instance, the residual magnetic bottle was in the previous magnetic moment run at $B_2 = 2.7(3)\,\mathrm{mT/m^2}$ and caused in the triple-trap magnetic moment measurement the dominant systematic uncertainty of $\Delta g/g = 0.97\,\mathrm{p.p.b.}$. The redesign of the trap stack reduces the expected inhomogeneity by a factor of ≈10, which will reduce the previous dominant limitation in future magnetic moment measurements by a similar factor. To determine the leading order components of the inhomogeneous magnetic field we apply the methods described above and documented in [3] in detail. Results of the cyclotron frequency measurements as a function of

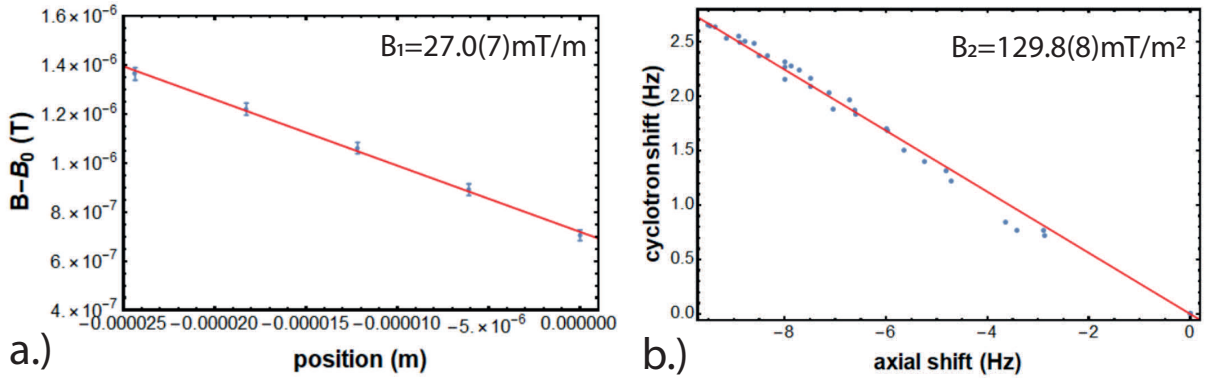

Figure 19: a.) Magnetic field as a function of particle position, from these measurements, based on single particle cyclotron frequency measurements as a function of position, we extract $B_1 = 27.0(7)\,\mathrm{mT/m}$. b.) cyclotron frequency shift as a function of axial frequency shift from simultaneous frequency measurements with a single particle. Based on the scaling and the independent determination of B_1, we obtain $B_2 = 129.8(8)\,\mathrm{T/m^2}$.

position are shown in Figure 19. From these measurements we obtain the magnetic field gradients shown in Table 8. Compared to the previous magnetic moment experiment [19], the linear gradient improved

Property	Value 2021	Value 2017
B_1	0.0270(7) T/m	0.0712(4) T/m
B_2	0.1298(8) T/m^2	2.7(3) T/m^2

Table 8: Comparison of magnetic field inhomogeneities in the precision trap of the last magnetic moment measurement and the current apparatus, which was designed to improve the previous measurement by a factor of 5 to 10.

by a factor of 2.6, the redesign of the trap stack reduced the magnetic bottle term in the precision trap by about a factor of 21.

6.7 Persistent Coil System

Although we have already sufficiently reduced the magnetic field inhomogeneity with the upgrades described above for an improved measurement of the antiproton magnetic moment, the newly implemented

local persistent magnet system allows for further reduction of the magnetic field gradients. In addition, tuneability of the B_2 term in the precision trap allows for important systematic studies, supporting temperature measurements, or moment measurements as a function of bottle strength B_2, which are all of utmost importance for the planned improved determination of the antiproton magnetic moment.

6.7.1 Development of the Coil System

At the beginning of 2021 the coil system was developed and tested in the BASE offline laboratory. This contained thermalization studies, thermal shielding studies, the development of reliable persistent joints as well as loading joints, and electronics to implement the persistent coil system into the experiment. The

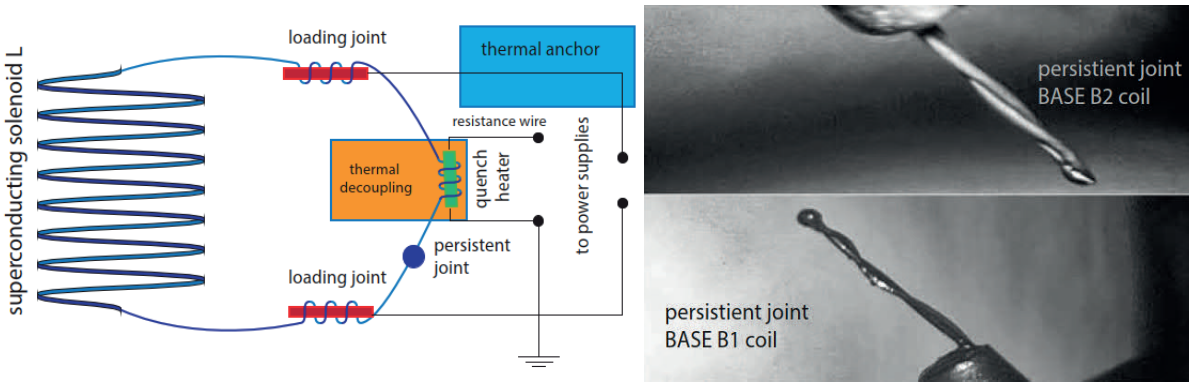

Figure 20: Left: Concept of implementation of the coils. Right: persistent joints made by spot welding.

left-hand side of Figure 20 shows the concept of persistent loading. The wires of the superconducting coil are connected with a persistent joint to form a superconducting loop. Two loading joints are present, connecting two points of the coil to an external current source. A thermally isolated quench heater is used to quench the superconducting wire locally, along the short path between the two loading joints. To load the coil, this heater is switched on, quenching the short path, and current is supplied to the coil via the loading joints. The coil will act as an LR circuit and current will build up through the windings of superconducting solenoid. Then, the quench heater is switched off and the interconnecting path is allowed to re-thermalize, becoming superconducting again. The current will continue to flow through the solenoid due to conservation of flux instead of taking the short path between the loading joints. Next, the current source is switched off and the current that was flowing through the solenoid will stay in the persistent loop, again due to conservation of flux. This loading concept is possible because the inductive reactance of the coil counteracts current decay via the resistor. Care must be taken when setting up the coil system: power dissipation through the loading joints needs to be low, and crosstalk between the loading joints and the quench heater needs to be avoided. The manufacturing of reliable loading joints is a challenge, it took several iterations until the ability to produce reliable loading joints was developed. To produce the persistent joints, we eventually used a spot-welding microscope. Photographs of working joints are shown on the right in Fig. 20.

6.7.2 Characterization of the B_1-Coil

To characterize the B_1 coil system, we load a single particle into the precision trap and measure the cyclotron frequency of the particle as a function of position. The particle position in the trap is adjusted by adding offset potentials to the trap electrodes and calculating the well-understood position/offset transfer function. Results of B_1 measurements as a function of the current applied to the coil are shown on the right-hand side of Figure 21. The blue datapoints represent B_1 measurements for constant current

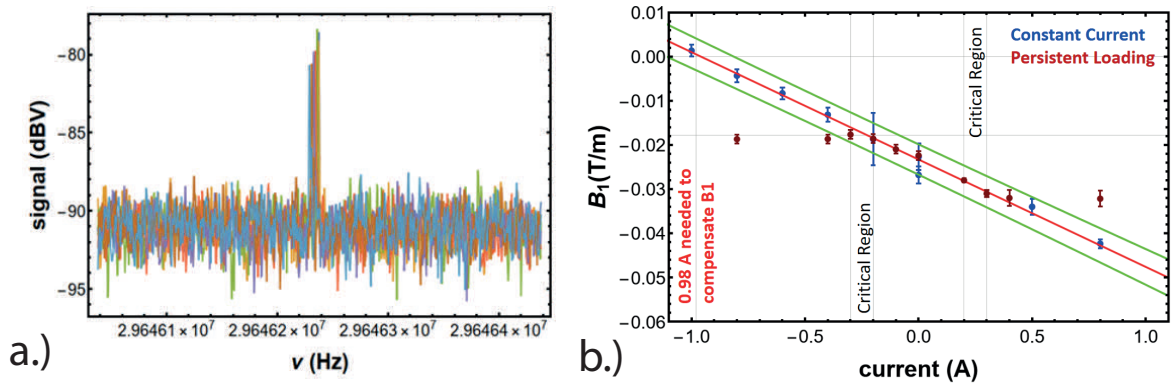

Figure 21: a.) Cyclotron frequency measurements as a function of particle positions. b.) Measured B_1 coefficient as a function of current applied to the B_1 coil. Blue data points for constant current supply, dark red data points for persistent currents.

applied via the coil's current supply. The B_1 coefficient can be tuned as expected, with a linear transfer function that is close to the design value. Once a persistent current is loaded into the coil, we obtain the results represented by the dark red data points. The persistent currents which survive inside the coil decay, independently of the loading attempt, to a value of about 270 mA. Our current understanding is that the reason for that behaviour is that the persistent joint of the B_1-coil has a low critical current density and is therefore not able to carry higher currents. Effectively we are able to tune the B_1 term of the trap to $B_1 = 18$ mT/m, 4 times lower than in the previous magnetic moment measurement, limited by the joint. Additional work is required to increase the current, which will be tackled in 2022. Note however, that the B_1-term is, apart from voltage drifts, not of any considerable systematic concern for trap systematics since the contribution averages out while the particle is oscillating over the gradient.

6.7.3 Characterization of the B_2-Coil

To characterize the B_2 coil, we perform simultaneous axial and cyclotron frequency measurements, for different modified cyclotron energies E_+. The measured scaling $\nu_+(\nu_z)$ together with the independently measured parameter B_1 enables a determination of B_2, as described in [3]. Results are shown

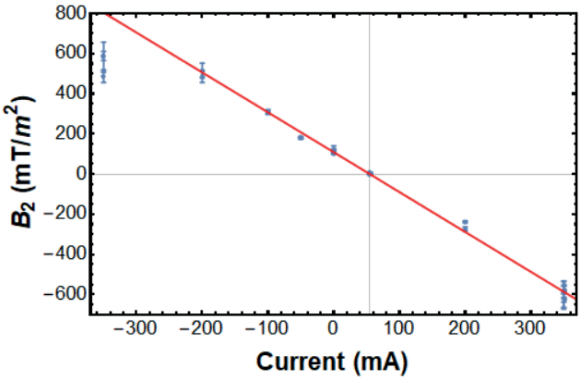

Figure 22: Measured magnetic bottle coefficient as a function of the current applied to the B_2 coil. With a current of 54.7(5) mA the B_2 coefficient of the trap can be tuned out.

in Figure 22, where we clearly demonstrate the inversion of the magnetic field bottle at a current of 54.7(5) mA, which means that a tuning $B_2 \approx 0$ can be achieved. A detailed characterization of our ability to tune this parameter to zero is in progress, at the moment we estimate the related uncertainty to

$\Delta B_2 \approx 0.0006\,\mathrm{T/m^2}$. Tuning of the magnetic bottle coefficient to this level would allow us to eliminate any B_2 related systematic uncertainty to be more than a factor of 100 below the target precision of the next magnetic moment measurement, which is at a level of ≈100 p.p.t.. The successful demonstration of the operation of the B_2 coil with a tuning range of $\pm 600\,\mathrm{mT/m^2}$ is, given that all the detectors are working properly, one of the most important results of the current run, it will enable us to perform antiproton magnetic moment measurements without B_2 related systematic uncertainty, which was the dominant systematic limitation of the previous measurement [19]. Although this looks promising, several additional commissioning experiments need to be carried out, for example the stability of the B_2 coefficient as a function of time after loading as well as the reproducibility of $B_2(I_c)$ need to be carefully characterized.

6.8 Axial Detection Systems of the Analysis Trap and the Cooling Trap

The axial detection systems form the interface between the single trapped particles and the experimentalists. Apart from the traps and a stable superconducting magnet, these devices are the most important interface elements of the BASE experiments. In this run BASE operates for the first time a four trap experiment. Also in the other traps, the analysis trap and the cooling trap, the developed axial detection systems show excellent performance. Figure 23 shows FFT-spectra of the axial detection systems of

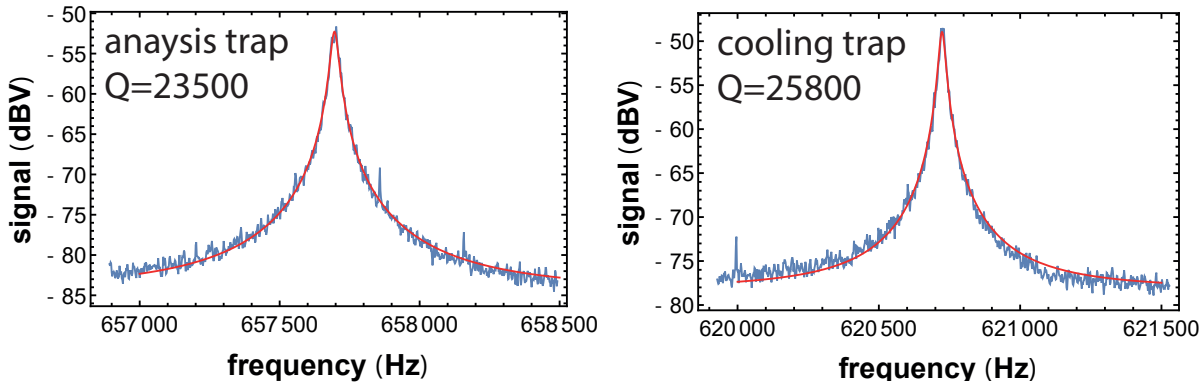

Figure 23: Axial detection systems of the analysis trap (left) with a quality factor of 23500 and the cooling trap (right) with a quality factor of 25800. Both detectors show a signal-to-noise ratio of about 30 dB, excellent for single particle detection and efficient frequency measurements.

the analysis trap and the cooling trap. For both detectors Q-values > 20000 are achieved at detection signal-to-noise ratios of ≈ 30 dB, similar to the detector of the precision trap with which axial frequency measurements with 30 mHz resolution within averaging times of ≈ 30 s can be performed.

6.9 Particle Transport and Detection of Particles in the Analysis Trap and the Cooling Trap

To close the experimental summary part of this report, we quickly flash results of efforts related to the currently ongoing commissioning and characterization measurements. The next step, after the successful commissioning of the precision trap, which is summarized above, is to implement particle transport along the entire 4 Penning trap stack and to commission the analysis trap and the cooling trap. First results of these commissioning measurements are shown in Figure 24, the left shows a single particle in the analysis trap, the plot on the right-hand side a single particle in the cooling trap. The peak signatures are produced by the response of the particle to a parametric excitation, injected to the trap at $2\nu_z$. Much work needs to be done to commission and characterize these traps, but the current status of the commissioning looks promising.

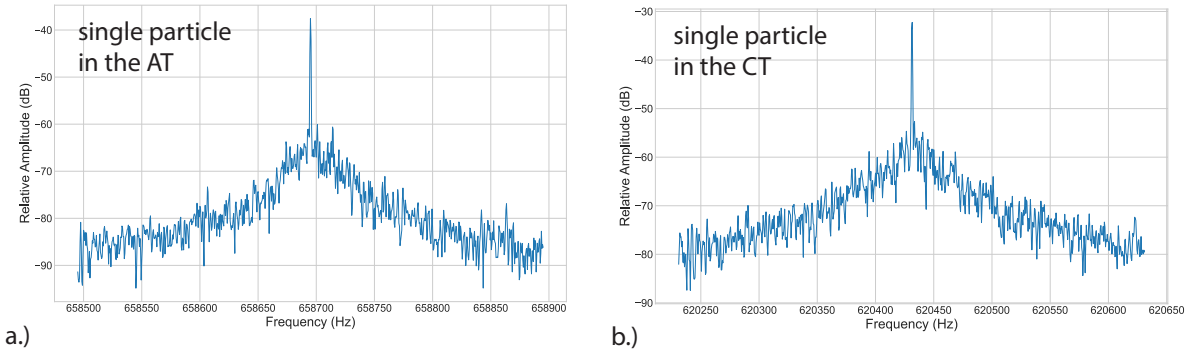

Figure 24: Detection of single particles in the traps of the new trap stack. Left: parametric resonance excitation of a single trapped particle in the analysis trap, and right in the cooling trap.

7 Parallel Developments

We operate the laboratory such that while a part of the team is responsible for measurements with the main experiment, another part develops devices for future runs. Here we summarize progress on the development of additional magnetometry, the installation of a new magnet logger system, the development of a new electron gun for the 2022 antiproton run and a 7-electrode Penning trap that is developed for the next charge-to-mass ratio comparison using phase-sensitive detection techniques.

7.1 Development of a New 7-Electrode Trap

Both a homogeneous magnetic field and a quadratic electric potential are needed to establish a reliable Penning trap for precision measurements. While the magnetic field is supplied by an external superconducting magnet, the quadratic electric potential can be approximated by different electrode geometries. Hyperbolic and cylindrical Penning trap designs have been implemented by several experiments. All Penning traps used by the BASE collaboration so far relied on a symmetric, cylindrical five-electrode design. The central ring electrode and a pair of compensation electrodes are supplied by ultra-precise power supplies with constant voltages, differing by a symmetric tuning ratio, while the pair of endcap electrodes are grounded. Besides the chosen trap geometry, satisfying the orthogonality condition, the five-electrode configuration allows local electrostatic compensation of a realistic trap. The tuning ratio acts as an externally controlable degree of freedom and is used to nullify the next-to-zeroth order term in the electric potential series expansion as a function of the axial coordinate. The absence of this term increases the harmonicity of the trap by reducing the axial frequency shift for small oscillation amplitudes (c.f. Duffing equations).
It is shown by the theory and confirmed by the measurements that higher order terms introduce significant anharmonicities for particles excited to larger axial amplitudes or higher magnetron radii. A new generation, seven-electrode precision trap would have an extra pair of correction electrodes with an additional independent voltage tuning ratio, resulting in one more degree of freedom, which could be used to locally compensate one more term in the electric potential power expansion. This was shown with seven-electrode traps already implemented by other collaborations (LIONTRAP and ALPHATRAP). Such a trap has the potential to further improve the precision of the BASE experiment and, with an increased trap radius, can open prospects for new measurement methods at enhanced resolution. For instance, a two-particle off-axis run would be made possible due to the increased workable magnetron region with relatively small frequency shifts. Such an upgrade can be expected to improve the precision in the q/m measurement. The cross-section view of the future trap design is shown in Figure 25 a). The COMSOL simulation of the quadratic electric potential with applied optimal tuning ratios is displayed

in Figure 25 b). Below, we will present additional technical aspects of the possible seven-electrode trap project.

The trap geometry is calculated by solving a number of simultaneous equations for coefficients C_j

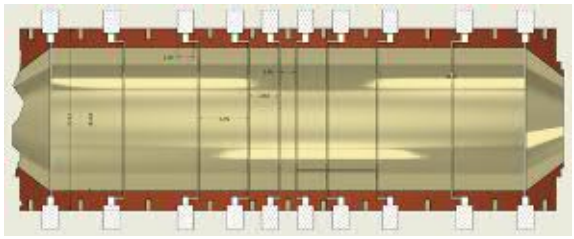

a) Seven-electrode trap cross section

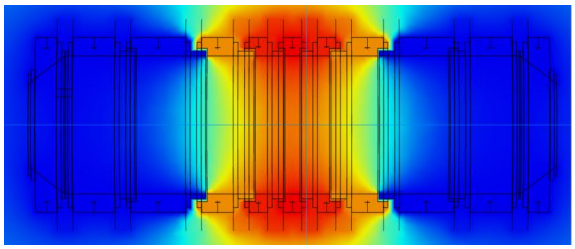

b) Quadratic potential simulation

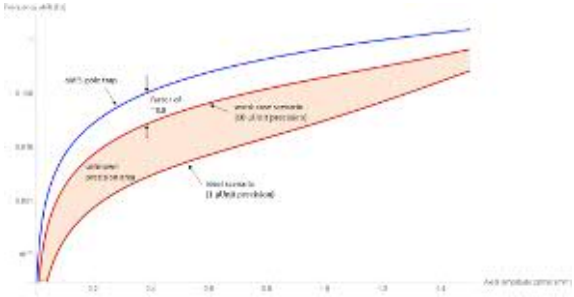

c) Axial trap anharmonicity

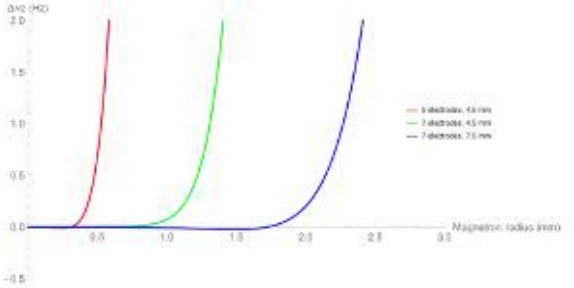

d) Magnetron trap anharmonicity

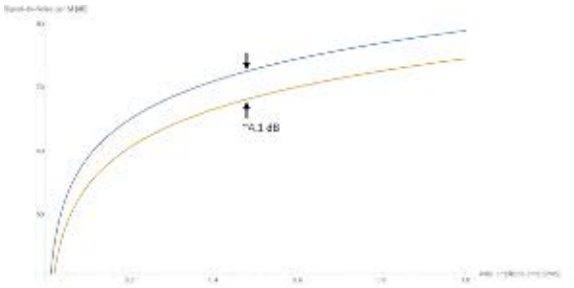

e) Signal-to-noise ratio upgrade

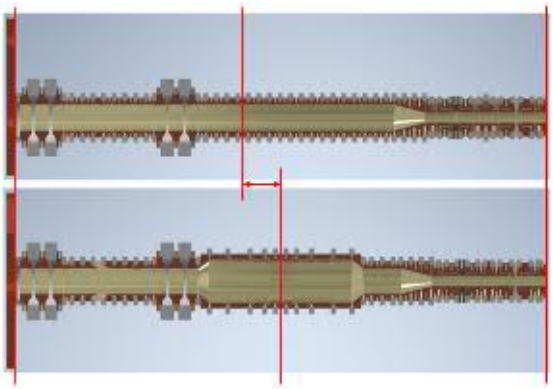

f) Trap stack comparison

Figure 25: Details of the seven-electrode trap being developed at BASE.

(even terms in the potential series expansion) and D_j (C_j derivatives with respect to tuning ratios) to be zero. No solution for the condition with independent $D_{2,1}$=0 and $D_{2,2}$=0 was achieved by numerical methods which is consistent with findings from other collaborations. If instead $D_{2,combined} = D_{2,1} \times TR_1 + D_{2,2} \times TR_2 = 0$ condition is used, a solution is possible with compact and implementable electrode geometries. The individual electrode dimensions were found by solving layout equations for C_4=C_6=C_8=C_{10}=0 at 7.5 mm trap radius, which gived the following electrode lengths: ring electrode 1.641 mm, inner correction electrode 3.068 mm, outer correction electrode 5.102 mm.

And endcap electrode stability analysis shows that the endcap length of 15 mm (twice the radius) will give the fractional correction to the electrode dimensions and tuning ratios of orders 10^{-5} – 10^{-3} which are comparable to copper electrodes and sapphire rings manufacturing tolerances ($\pm$ 5 – 10 µm) and thermal contraction effects (Cu coefficient 1.0032). It was shown by explicit simulation of the axial frequency shift as a function of the magnetron radius that thermal contraction effects on trap harmonicity would be within the manufacturing tolerances, therefore, there is no need to adjust the designed values for that. The 140 µm spacings between the electrodes were left unchanged from the previous version. The sapphire rings used to hold the electrodes in the precision trap will be manufactured with ±5 µm

precision. The OFHC electrodes are yet to be ordered. The electrodes will be silver- and gold-coated for up to 15 µm thickness.
The realistic trap electric field harmonicity was investigated more in detail. First, the robustness of the inner and outer tuning ratios was considered with an offset of ±50 µm for the electrode lengths, spacings between neighboring electrodes, and the trap radius. In all cases, local compensation, such that the coefficients C_4 and C_6 are nullified, was found possible. Realistically, these coefficients will be limited by the output of the power supplies. This leads to a small residual level of C_4 and C_6 as well as non-zero values of C_8 and C_{10}. The "worst case scenario" investigation was carried out further, considering the manufacturing imperfections to add up in a non-compensating way. Thermal contraction as the system undergoes a cool down from room temperature ∼300 K to the operating point of ∼4 K was also considered. This leads to the axial frequency shift due to finite axial amplitude. The comparison with the current trap is given in Figure 25 c). The curve for 1 µV power supply reliability is also given in the plot. We expect a real seven-electrode trap to have an axial frequency shift in the pink region.
The axial frequency of protons/antiprotons in the precision trap is limited by the increase of the precision trap radius from currently 4.5 mm to 7.5 mm, and the maximum output voltage available by the power supplies (14 V). For this reason the operational axial frequency will be downshifted from the current 650 kHz to the new frequency of 500 kHz, which is feasible to implement by building a new resonator. The corresponding new ring voltage will be about 10.16 V. The increased effective cyclotron electrode distance will be resolved by picking-up at both inner and outer correction electrodes. Finally, the axial frequency shift as a function of magnetron radius was simulated. The comparison of the currently used five-electrode 4.5 mm radius trap, a hypothetical 4.5 mm trap with seven electrodes, and the newly designed trap is given in Figure 25 d). In order to get a more informative comparison, the axial frequency in all cases was downshifted to 500 kHz.
The length of the precision trap after the upgrade will increase by 26.4 mm which effectively shifts the center of the precision trap. This suggests that a new self-shielding tuning coil system will need to be implemented symmetric with respect to the center of the new PT ring electrode. In order to keep the same trap stack length, the transport section between the precision trap and the analysis trap will need to be contracted. The on-axis magnetic field for the new trap stack was simulated with COMSOL. This change was found to increase the magnetic bottle at the centre of the PT caused by the ferromagnetic ring electrode of the AT by a factor of ∼2 to 0.759 T/m^2. Reversing the order of the CT and the AT was also considered. This would decrease the value of B_2 to 0.202 T/m^2, which is even lower than the one for the current trap configuration (0.349 T/m^2). The preliminary estimate of the peak signal-to-noise ratio is expected to increase by about 4.1 dB as we expect an axial resonator with better quality factor (∼50 000), see Figure 25 e). Cross sections of the trap stack with the old precision trap and with the designed seven-electrode precision trap are given in Figure 25 f).

7.2 Development of New Magnetometry

When performing comparisons of the antiproton-to-proton charge-to-mass ratio it is important that the magnetic field remains constant during and between frequency measurements. This is equally true when measuring the Larmor and cyclotron frequencies to determine the magnetic moment of the antiproton. Any fluctuations in the magnetic field directly reduce the precision to which we can measure these vital quantities. To combat magnetic field drifts caused by variations in the magnetic field of our superconducting magnet, or by thermal drifts of the apparatus within the magnet, BASE has significantly improved the mechanical stability and stabilisation of the magnet [45], and plans to go even further in the future [25]. A second source of magnetic field noise is caused by the antiproton decelerator, ELENA or other users in the Antimatter Factory. To better understand these fluctuations, we have constructed an array of 10 fluxgate magnetometers: 5 Stefan Mayer FLC3-70 3-axis sensors [49] and 5 Stefan Mayer FLC-100 1-axis low noise sensors [50] . The properties of the sensors are listed in Table 9. One sensor of each type

is placed in an enclosure as shown in Figure 26 a); four of these boxes are placed around the BASE Penning trap at the corners of a cuboid as indicated in Figure 26 b). The 5th sensor is placed in a mu-metal box next to the 4th sensor (magnetic shielding factors along x,y,z of 87,26,41 respectively), and provides a reference of the electronic noise floor of the magnetometers. The sensors are read out using a National

Property	FLC3-70	FLC-100
Axes	3	1
Range (μT)	$\pm$200	$\pm$100
Calibration (μT/V)	35	10
3dB Bandwidth (kHz)	0-1	0-1
Noise floor at 1 Hz (pT/$\sqrt{\text{Hz}}$)	120	20

Table 9: Properties of the Stefan Mayer FLC3-70 [49] and FLC-100 sensors [50]

Instruments PXIe-6363 multi-function ADC card. A custom breakout-box has been constructed to act as an interface between the magnetometers and the PXIe-6363. This can filter the incoming signals with time constants 0.11 s for the FLC-100 and 0.22 s for the FLC3-70 sensors, or using re-configurable jumpers the filters can be bypassed and the full bandwidth of the sensors used. The system is also designed so that, if necessary, magnetic compensation coils can be incorporated into each sensor box, also controlled by the PXIe-6363. The PXIe-6363 card is placed in our National Instruments datalogger computer [51]. The fluxgate array was installed at the end of the beamtime in 2021, a plot of the response of the system

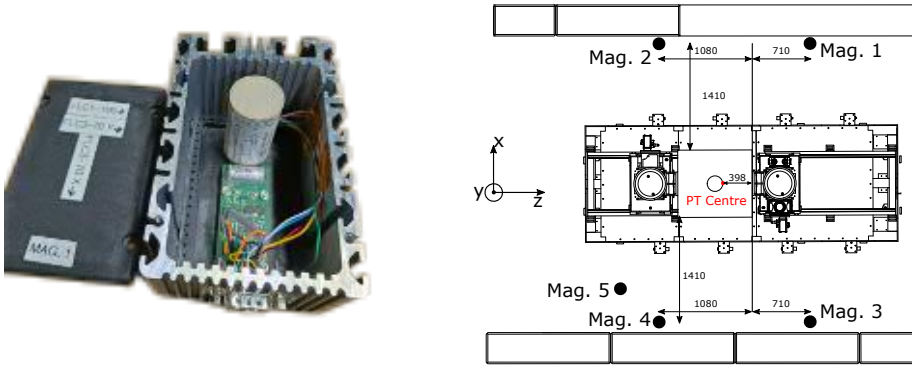

Figure 26: a) Photograph of the two sensors in an enclosure. b) Diagram of the location of the sensors relative to the BASE magnet and centre of the Precision Trap (PT). All dimensions in millimeters. The boxes labelled $1\,\&\,4$ are 920 mm below the magnet centre line and $2\,\&\,3$ are 1040 mm above this line. The box labelled 5 is at approximately the same height as 4 in a mu-metal box.

as the bridge crane passes overhead is shown in Figure 27. This type of magnetic disturbance occurs frequently as other users are active in the zone; for reference a 2 µT field change along the z axis without any shielding would lead to a 1 parts-per-million fluctuation in the cyclotron frequency, while we are attempting charge-to-mass ratio and magnetic moment comparisons 10^6 and 10^3 times better than this respectively.

7.3 Magnet Logger System

The superconducting magnet is an essential part of the experimental setup. It has a horizontal bore, in which the trap is placed, surrounded by a vessel for liquid helium (LHe) and liquid nitrogen (LN2) which

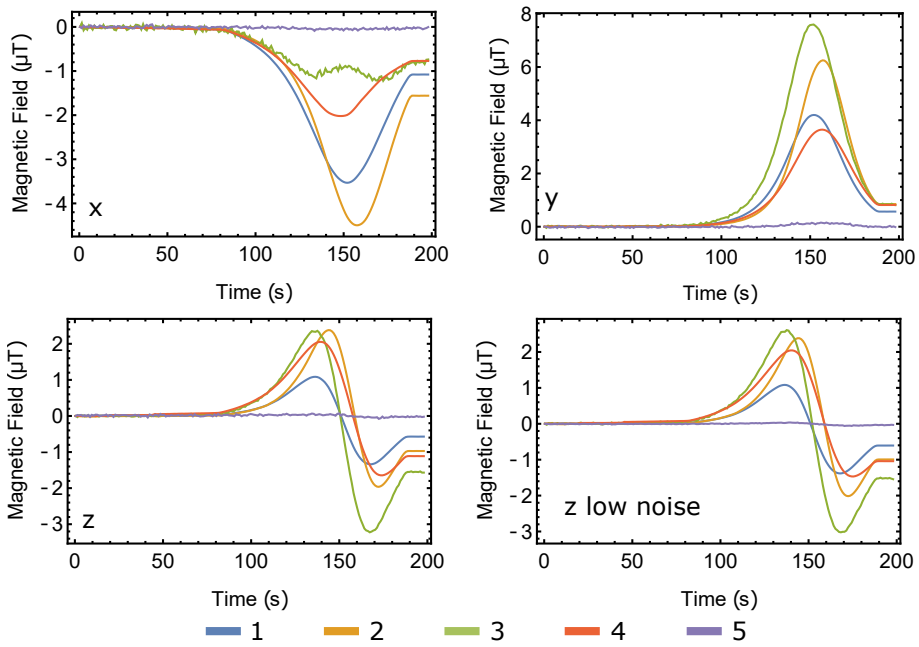

Figure 27: Magnetic field detected by the fluxgate sensors as the bridge crane passes overhead, axes as in Figure 26

cools the magnet coil below its critical temperature. A quench of the magnet corresponds to a delay in the experiment of several month, therefore, it is essential to continuously monitor the magnet's operation and parameters such as pressures in the insulation vacuum, helium and nitrogen evaporation flow. For this, we were setting up a battery based standalone logger system, which monitors the mentioned parameters. Figure 28 a) shows the newly implemented setup to monitor the pressure of the magnet. It consists

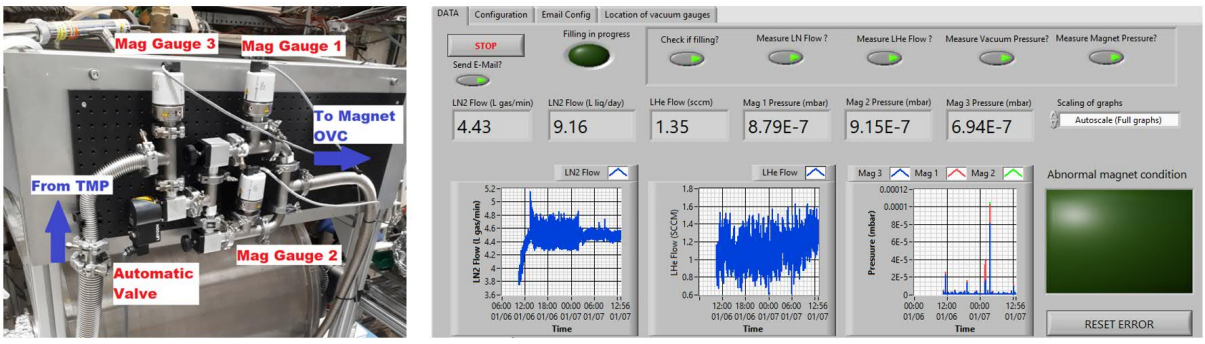

a) b)

Figure 28: a) Photograph of the setup to monitor the pressure in the superconducting magnet. b) LabView monitoring the LN2 flow, LHe flow and pressure from left to right.

of three redundant pressure gauges; one measuring the pressure of the vacuum coming from the turbo-molecular pump (TMP), the other two the pressure going to the outer vacuum chamber (OVC) of the magnet. Between these two and the other pressure gauge is an automatic valve, which closes in case of a power cut affecting the TMP.

The pressure and the flow of both the LN2 and LHe exhaust are recorded via a LabVieW VI shown in Figure 28 b). It also sends automatic e-mails in case the averaged flow or the averaged pressure drops or rises under or above a set value, respectively. During the filling of LN2, the respective flowmeter has to be disconnected. For this case we also implemented a switch, which tells the VI if the flowmeter

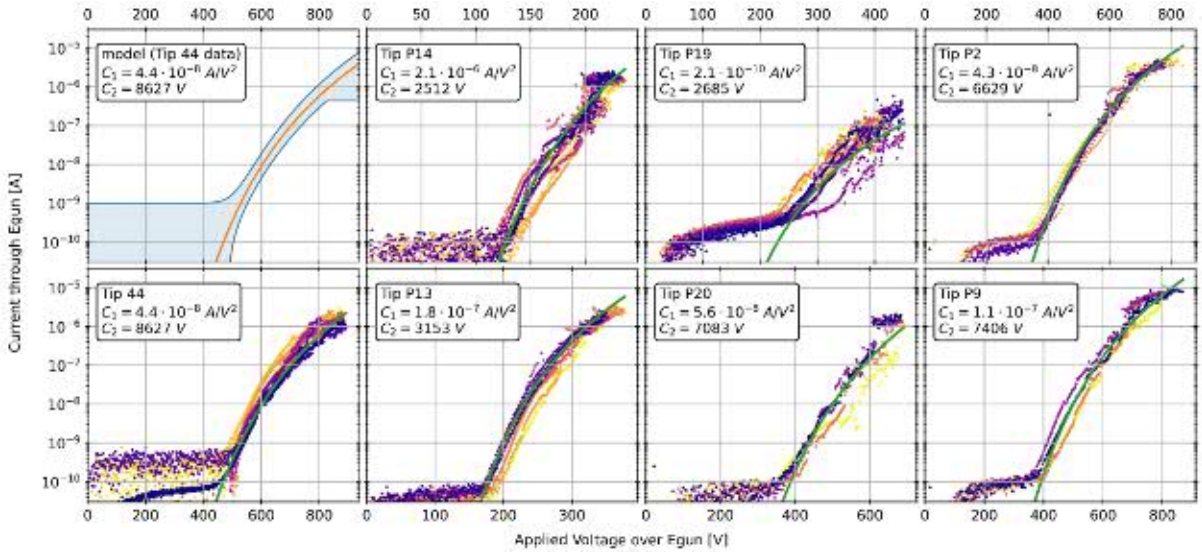

Figure 29: Electron current generated by the Field Emission Tip depending on applied voltage. Top Left: Emission model fitted to the data of tip 44 with $1\,\mathrm{nA}$ of noise and a magnitude of uncertainty. Others: Measured tip emissions and parameters of the model fit.

is disconnected, so no warning e-mails will be sent. The different limits and averaging times for the warning e-mails can be seen in Table 10.

Warning	Limit	Averaging time (s)
LN2 low flow	4 l gas/min	600
LHe flow low	not yet set (fluctuations in He recovery line)	86400
Pressure high	1E-5 mbar	300
LN2 flowmeter disconnected	2.5 l gas/min	21600
Filling switch	Filling enabled	25200

Table 10: Limits and averaging times for e-mail warning.

7.4 New Electron Gun

Field Emission Tips (FETs) are used in the BASE electron gun to produce hydrogen ions (p^+, H^-) and to provide electrons required for electron cooling of injected antiprotons. Sharper tips decrease the voltage needed to emit electrons and consequently increase the electron current at a constant voltage. Using the electron gun degrades the FETs over time, so new sharp tips needed to be produced. The FETs at BASE are made from pieces of tungsten wire that are sharpened by etching. Material is etched off of the wire – which functions as an anode – by galvanizing a copper cathode using sodium hydroxide as an electrolyte.

Wires with a diameter of $0.2\,\mathrm{mm}$ to $0.5\,\mathrm{mm}$ were used and etched with a 3-molar sodium hydroxide solution. Successfully etched tips were characterized in a small vacuum chamber at approximately 10^{-8} mbar by connecting a voltmeter and high voltage power supply in series. With those, the current and voltage drop over the electron gun can be calculated as $I_{\mathrm{Egun}} = U_{\mathrm{VM}}/R_{\mathrm{VM}}$ and $U_{\mathrm{Egun}} = U_{\mathrm{HV}} - U_{\mathrm{VM}}$ via the internal resistance R_{VM} of the voltmeter. The emission can be modeled by Fowler-Nordheim tunneling to provide a description of the current dependence on applied voltage:

$$I_{\mathrm{Egun}} \propto C_1 \cdot U_{\mathrm{Egun}}^2 \cdot e^{-C_2/U_{\mathrm{Egun}}}, \tag{13}$$

where the parameters C_1 and C_2 are constants containing the workfunctions of the material and some geometry factors. Figure 29 shows the measured current fitted with the Fowler-Nordheim model for all characterized tips. For comparison, the currently used electron gun requires $1.4\,\mathrm{kV}$ to generate $100\,\mathrm{nA}$ of current, the newly developed field emission tips operate at much lower acceleration voltage.

8 BASE-Mainz and BASE-Hannover Experiments

Cooling techniques play an essential role in the precision measurements of the BASE collaboration. In particular, energies as low as 100 mK in the cyclotron mode are essential for the unambiguous identification of the proton/antiproton spin state for magnetic moment measurements [19, 21]. Therefore, we have started efforts to include sympathetic cooling with laser-cooled ions into antiproton measurements: cooling based on separately trapped protons and beryllium ions via Coulomb interaction by the BASE-Hannover group [52] and via image-currents by the BASE-Mainz group [2, 53].

8.1 Sympathetic Cooling of Protons at the BASE-Mainz Experiment

In 2021, the experimental demonstration of cooling a single proton via image currents by the BASE-Mainz group was published in Nature [2]. Here, two Penning traps were used to separately confine a single proton and a cloud of up to about 200 beryllium ions. Energy exchange between the two traps was realized via a shared LC circuit that connected to one electrode in each of the traps. Usually we use the LC circuit as image-current detector to measure the axial frequency of the particles in both traps. However, if we match the axial frequency of the proton and beryllium ions, we create a coupled oscillator system where the particles exchange energy between the traps by their image-current interaction with the shared LC circuit. In addition, the LC circuit amplifies the induced voltage amplitude that causes coupling force between the trapped particles by its Q-factor so that the Rabi frequency is large (~ 1 Hz) compared to the frequency stability limit (~ 20 mHz). To cool the protons, we apply additional damping to the beryllium ions with a cooling laser. It is essential to carefully tune the photon scattering rate in these measurements, since the beryllium ions would either decouple from the system or not provide enough cooling power if the scattering rate was too high or too low, respectively. In this configuration, we reduced the axial temperature of the proton to about 15% of the LC circuit temperature that so far defined the axial temperature of the proton. The cooling process reaches a cooling time constant on the order of 1 s, which is more than a factor 100 faster than resistive cyclotron cooling.

The temperature limit of about 2.5 K in the previous run [2] was set by the Johnson noise of the LC circuit that competes with the cooling process. Since the temperature limit was not sufficient yet for an application of the method in a proton/antiproton magnetic moment measurement, it was necessary to develop a concept to be able to decrease the axial temperature by another factor of 100 to reach an axial temperature in the 10 mK range. That would enable the preparation of the cyclotron mode in the desired energy range. Further, the necessity to measure the proton temperature during the cooling procedure and the limited temperature resolution in the previous setup required us to prepare and install various technical upgrades and make major modifications to the experimental setup to be able to improve on the temperature limit. This work has been carried out in 2021 by the BASE-Mainz team.
A summary of the simulation work on the sympathetic cooling schemes has been recently submitted for review [54]. One essential modification of the cooling scheme is to detune the LC circuit from the common proton and beryllium ion axial frequency during the energy exchange. Since the heating rate scales approximately with δ^{-2}, whereas the coupling rate scales with δ^{-1} as function of the detuning δ, it is advantageous to operate with a detuned LC-circuit since the temperature limit improves even though the coupling rate of the trapped particles decreases. Figure 30 a) shows the temperature limit and the cooling time constant of a cooling scheme with multiple laser-cooling pulses and energy exchange peri-

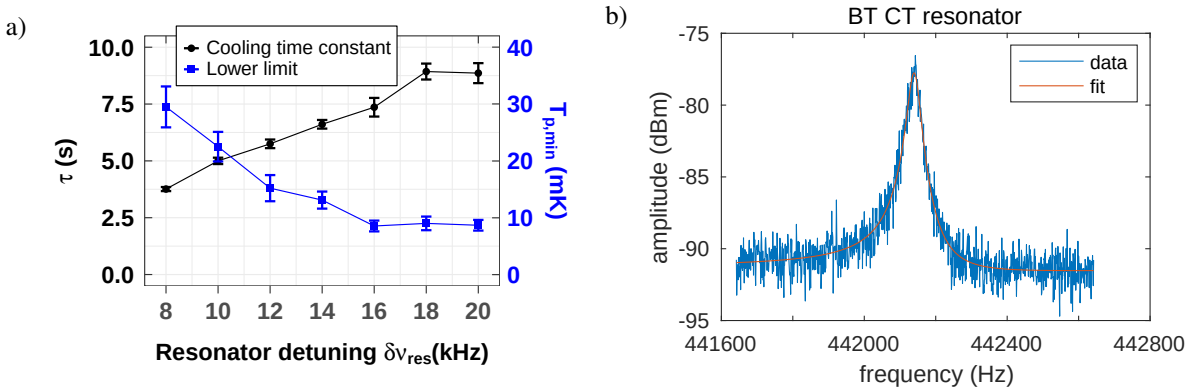

Figure 30: a) Simulation results of cooling a single proton with beryllium ions via a detuned LC-circuit. The cooling time and the temperature limit are shown as function of the detuning from the LC circuit frequency. Details are found in ref. [54]. b) FFT spectrum of the improved image-current detection system of the beryllium trap and the coupling trap, illustrating the improved Q-factor necessary to explore the 10 mK range in proton axial temperature.

ods between the coupled trapped particles as function of the frequency detuning of the common particle frequency from the one of the LC circuit. It is possible to reach 10 mK using a detuning of about 300 to 600 LC circuit linewidths.

The installation of the technical upgrades has been completed and the experiment was cooled down at the end of the year with the goal to demonstrate cooling in the 10 mK range in 2022. To this end, a new trap stack consisting of six Penning traps was assembled. Compared to the previous trap system, a dedicated temperature measurement trap was added that includes an about 10-fold weaker magnetic bottle compared to the spin-flip analysis trap. This provides faster temperature measurements with about 10 mK resolution and requires less time in commissioning. Further, a new loading trap for proton and beryllium ions was installed that enables the production of protons and beryllium ions from two separate laser ablation targets. Thereby, the two particle species are produced with a lower amount of contamination which reduces the trap reloading time. Of particular importance here is that the trap geometry has no direct line of sight between the targets and the neighbouring traps, so that loading ions does not cause potential shifts in the other traps by material deposition on the trap surfaces. These upgrades will avoid many technical difficulties encountered in the operation of the previous trap system. Another essential upgrade was the improvement of the image-current detection systems to higher Q-factors. In particular, the Q-factor of the coupling trap needed to be improved to reduce the temperature limit in the new coupling procedure. To this end, the detectors and the trap system were tested in a cold head installation without magnetic field, where all components that potentially affect the Q-factor of the LC circuit were improved until a Q value of 20 000 was reached. The operation in the magnetic field reduces the Q-factor to 12 000, see Figure 30 b), which is a factor 6 improvement compared to the previous run and will suffice to explore the 10 mK range. The optimization work includes also the installation of a loss-free tunable capacity that shifts the LC circuit frequency by up to 20 kHz using a commercial cryogenic piezo-motor, which was not available in the last run and is essential to reach a lower temperature.

We expect to observe coherent energy exchange between the proton and beryllium axial amplitudes, and explore the temperature range down to the 10 mK range in the year 2022. If successful, we expect that the technique will be sufficiently developed to be applied in the next proton magnetic moment measurement in the BASE-Mainz trap system, and with a revised trap system with laser access, also in future antiproton measurements of the BASE collaboration at CERN.

8.2 Summary BASE Hannover 2020

At the BASE Hannover experiment, we are working on an experimental method inspired by quantum logic techniques that could improve particle localization and readout speed. The method allows for sympathetic cooling of the (anti-)proton to its quantum-mechanical ground state as well as the readout of its spin alignment. Both of these features are achieved through coupling to a laser-cooled 'logic' ion which is co-trapped in a double-well potential. This technique is similar to the BASE-Mainz experiment in some aspects but will provide much higher coupling rates and enables more sensitive particle manipulation schemes due to the used double-well potential. This will boost the measurement sampling rate by orders of magnitude and will thus provide results with a lower statistical error and could contribute to a stringent search for sidereal variations in the data. Such measurements ultimately yield extremely high sensitivities to many baryonic coefficients in the Standard-Model Extension [40] and allow the exploration of previously unmeasured types of symmetry violations. In 2021, we have published a full proposal on the implementation and implications of sympathetic laser cooling and quantum logic spectroscopy for precision spectroscopy on single (anti-)protons [55]. We have used the novel 140 GHz Raman laser system to observe spin-flip transitions in a cloud of trapped $^9Be^+$ ions. By implementing a wave vector difference of both phase-coherent 140 GHz split UV laser beams along the axial direction of the trap, we have been able to perform thermometry on the cloud and obtain an axial temperature of 1.77 mK as a result of Doppler cooling [56]. We have significantly improved the control over single ions and have been able to observe spin-motional sideband transitions that add or substract one quantum of axial motion while flipping the spin of the ion. In combination with spin-resetting resonant repumping transitions, this has allowed the realization of sideband cooling to the absolute motional ground state of the axial motion. To our knowledge, we are only the third group worldwide achieving optical sideband cooling to the motional ground state in a Penning trap. Furthermore, we have been able to use both Doppler-recooling and Raman spectroscopy to characterize motional excitation during ion transport and have, at the level of sensititivity, not found any transport-induced motional heating yet.

9 Summary on Experimental Progress

We have summarized the progress made by the BASE collaboration in 2021. While several manuscripts in visible scientific journals were produced, which were summarized in this report, the team produced considerable progress with:

- The development of a broad band high-Q superconducting detector which will increase the bandwidth of future BASE efforts to search for axions by more than a factor of 1000 in bandwidth and at improved detection sensitivity.
- The successful setup of an interface which connects BASE to ELENA. We have demonstrated that the interface allows sufficient transmission in a foil range with a width thickness of about 1760 nm. The currently used foil is able to hold the vacuum to provide conditions sufficient to store single antiprotons for $>$ 3 months. With the reservoir trap which usually stores up to 1000 particles continuous experiment operation during accelerator shutdown periods will be possible.
- The newly developed 4 trap system is performing very well. The superconducting particle detectors were commissioned successfully, all the devices have sufficient detection sensitivity to conduct efficient single particle experiments. Transport through the entire trap stack was demonstrated and single particle signals were observed in all traps that are required for the planned magnetic moment measurements. The newly implemented superconducting shim coil system was commissioned successfully. While the less important B_1 coil requires one additional more iteration, the B_2 coil tuning range is sufficient to tune $B_2 \approx 0$, which will eliminate the dominant systematic uncertainty of the previous magnetic moment measurement and will allow for a new class of systematic

studies.

10 Projects for the 2022 run

Continued commissioning of an experiment to measure the antiproton magnetic moment with a fractional precision of ≈ 100 p.p.t.

11 Funding

BASE is supported by the RIKEN chief scientist program (Ulmer), the RIKEN pioneering project program (Ulmer/Yamazaki), the RIKEN SPDR (Wursten, Latacz) and JRA (Fleck) programs, an ERC starting grant for the implementation of quantum logic methods (Ospelkaus), and an ERC starting grant for the implementation of the transportable trap (Smorra). In addition, several of the BASE co-workers are supported by fellowships. The collaborating institutes (MPI-K, Univ. Hannover/PTB, ETH Zuerich, and Univ. Mainz) contribute funding for and supervision of the BASE PhD-students (Blaum / Walz / Ospelkaus / Quint / Soter).
Currently the collaboration funding is secured, further details on available research funds can be presented on request.

12 Collaboration and Manpower

We are happy to welcome ETH Zuerich as a new collaborating institute (Prof. Dr. Anna Soter). With this new collaboration member BASE consists now of 10 collaborating institutes and universities which send students and post docs to operate the CERN experiment. The CERN experiment is typically operated by

- RIKEN: 1 P.I., two post docs, students which are usually supported by RIKEN's junior scientist programs (JRA, SPDR, FPR) and students from international joined programs. Due to the restrictive COVID policy of the Japanese government manpower-supply from Japan is currently reduced. In addition some BASE post-docs are expected to spend in 2022 extended time periods in Japan, which will potentially affect the operation of the 2022 antiproton run.
- MPIK: two PhD students or one post doc, one PhD student.
- LU-Hannover / PTB: one PhD student / MA and BA students (typically 2).
- University of Tokyo: under discussion (see COVID policy of Japan).
- JG-Mainz / HIM Mainz: 1 PhD or MA student.
- GSI: 1 MA student.
- CERN: Currently CERN supports BASE via one PhD student (Gentner Program, Jaeger), one fellow (Micke), and one LD position (Devlin).

The current manpower-availability is sufficient to secure the operation of the BASE-CERN experiment in the AD hall.
The BASE collaboration partners will secure continued operation of the BASE experiments under comparable conditions as described above.

13 Explicit Requests

In 2022 BASE will be expanded by the second experiment BASE-STEP. The STEP team will send up to three persons permanently to CERN, office space for these three persons is required. Although in

the office building 545 two offices are practically not in use and we were asking to allocate one of these offices to BASE, no communication was possible with the responsible group at CERN. We ask our referees to support our request to get one of the available offices in building 545 with considerable momentum.

14 Acknowledgments

We would like to thank the committee and our reviewers for the invaluable time invested to evaluate this report. We acknowledge technical support of the Antiproton Decelerator group, CERN's cryolab team, and all other CERN groups which provide support to Antiproton Decelerator experiments.
We would like to thank the other AD collaborations for many fruitful discussions, continuous support, friendship and the inspiring coexistence at CERN's antiproton decelerator facility.
We would like to explicitly express our empathic gratitude to CERN for promoting the BASE technical coordinator Jack A. Devlin to one of the highly competitve LD positions!
We acknowledge financial support by RIKEN's Chief Scientist Program, RIKEN Pioneering Project Funding (EEE), the RIKEN-JRA Program, the RIKEN-FPR Program, the Max-Planck Society, CERN's fellowship program, CERN's Gentner Program, the Helmholtz-Gemeinschaft, the DFG through SFB 1227 'DQ-mat' (grant ID 274200144), the European Research Council (ERC) (Grant agreement No. 852818, No. 337154 and No. 832848), and the Max-Planck–RIKEN–PTB Center for Time, Constants and Fundamental Symmetries,

Bibliography

[1] J. A. Devlin et al., Physical Review Letters **126**, 041301 (2021).
[2] M. Bohman et al., Nature **596**, 514 (2021).
[3] M. J. Borchert et al., Nature **601**, 53 (2022).
[4] S. Depanfilis et al., Physical Review Letters **59**, 839 (1987).
[5] S. Ulmer, *First observations of spin flips with a single trapped proton*, PhD thesis, Univ. Heidelberg, 2011.
[6] S. Ulmer et al., Nature **524**, 196 (2015).
[7] R. Lehnert, Symmetry **8**, 114 (2016).
[8] S. Ulmer et al., Physical Review Letters **106**, 253001 (2011).
[9] C. Smorra et al., International Journal of Mass Spectrometry **389**, 10 (2015).
[10] C. Smorra et al., The European Physical Journal Special Topics **224**, 3055 (2015).
[11] S. Ulmer et al., Review of Scientific Instruments **80**, 123302 (2009).
[12] S. Ulmer et al., Nuclear Instruments and Methods in Physics Research Section A **705**, 55 (2013).
[13] H. Nagahama et al., Review of Scientific Instruments **87**, 113305 (2016).
[14] J. DiSciacca et al., Physical Review Letters **110**, 130801 (2013).
[15] H. Nagahama et al., Nature communications **8**, 1 (2017).
[16] C. Smorra et al., Physics Letters B **769**, 1 (2017).
[17] S. Sellner et al., New Journal of Physics **19**, 083023 (2017).
[18] S. Ulmer, A. Mooser, H. Nagahama, S. Sellner, and C. Smorra, Philosophical Transactions of the Royal Society A: Mathematical, Physical and Engineering Sciences **376**, 20170275 (2018).
[19] C. Smorra et al., Nature **550**, 371 (2017).
[20] A. Mooser et al., Nature **509**, 596 (2014).
[21] G. Schneider et al., Science **358**, 1081 (2017).

[22] M. Borchert et al., Physical Review Letters **122**, 043201 (2019).
[23] J. A. Devlin et al., Physical Review Applied **12**, 044012 (2019).
[24] C. Smorra et al., Nature **575**, 310 (2019).
[25] S. Ulmer et al., Future Program of the BASE Experiment at the Antiproton Decelerator of CERN, Technical report, CERN, Geneva, 2019.
[26] G. Gabrielse and J. Tan, Journal of Applied Physics **63**, 5143 (1988).
[27] F. Heiße et al., Physical Review Letters **119**, 033001 (2017).
[28] G. Gabrielse et al., Physical Review Letters **82**, 3198 (1999).
[29] E. G. Myers, International Journal of Mass Spectrometry **349**, 107 (2013).
[30] M. Charlton, S. Eriksson, and G. Shore, Testing fundamental physics in antihydrogen experiments, Preprint at `https://arxiv.org/abs/2002.09348`, 2020.
[31] R. J. Hughes and M. H. Holzscheiter, Physical Review Letters **66**, 854 (1991).
[32] R. J. Hughes, Physical Review D **41**, 2367 (1990).
[33] I. Kenyon, Physics Letters B **237**, 274 (1990).
[34] C. Tchernin, E. T. Lau, S. Stapelberg, D. Hug, and M. Bartelmann, Astronomy and Astrophysics **644**, A126 (2020).
[35] G. Chardin and G. Manfredi, Hyperfine Interactions **239**, 1 (2018).
[36] K. Abe et al., Physical Review D **95**, 012004 (2017).
[37] P. Perez and Y. Sacquin, Classical and Quantum Gravity **29**, 184008 (2012).
[38] W. A. Bertsche, Philosophical Transactions of the Royal Society A: Mathematical, Physical and Engineering Sciences **376**, 20170265 (2018).
[39] P. Scampoli and J. Storey, Modern Physics Letters A **29**, 1430017 (2014).
[40] V. A. Kosteleckỳ and N. Russell, Reviews of Modern Physics **83**, 11 (2011).
[41] Y. Ding and M. F. Rawnak, Physical Review D **102**, 056009 (2020).
[42] C. Smorra et al., Technical Design Report of BASE-STEP, Technical report, CERN, Geneva, 2021.
[43] F. Volksen, *Bachelor Thesis*, PhD thesis, 2021.
[44] H. Häffner et al., The European Physical Journal D-Atomic, Molecular, Optical and Plasma Physics **22**, 163 (2003).
[45] M. Borchert, *Challenging the standard model by high-precision comparisons of the fundamental properties of protons and antiprotons*, PhD thesis, Leibniz University of Hannover, 2020.
[46] W. Hassenzahl and W. Gray, Cryogenics **15**, 627 (1975).
[47] J. Engel et al., AIP Advances **10**, 025224 (2020).
[48] S. P. Møller et al., Physical Review Letters **88**, 193201 (2002).
[49] Stefan Mayer Instruments, *Magnetic Field Sensor FLC3-70*.
[50] Stefan Mayer Instruments, *Fluxgate Sensor FL1-100*.
[51] A. L. Ponten, BASE Data Logger, Technical report, 2019.
[52] M. Niemann et al., Measurement Science and Technology **31**, 035003 (2019).
[53] M. Bohman et al., Journal of Modern Optics **65**, 568 (2018).
[54] C. Will et al., Sympathetic cooling schemes for separately trapped ions coupled via image currents, 2021, arXiv/2112.04818.
[55] J. M. Cornejo et al., New Journal of Physics **23**, 073045 (2021), Publisher: IOP Publishing.
[56] J. Mielke et al., Journal of Physics B **54**, 195402 (2021), Publisher: IOP Publishing.